Influence of turbulence-kernel interactions on flame development in lean methane/air mixtures under natural gas-fueled engine conditions

Harinath Reddy and John Abraham*
School of Mechanical Engineering, Purdue University, West Lafayette, IN

Abstract

Direct numerical simulations (DNS) with reduced chemistry are carried out to study the influence of flow velocity and length scales on flames developing from flame kernels in lean methane/air mixtures. This study is conducted at elevated temperature and pressure conditions relevant to lean-burn natural gas engines. There are two effects which come into consideration: the interaction of turbulence with the kernel and the interaction with the local flame. A range of scales is selected so that interactions in different regimes can be studied. A flame surface density (FSD) approach is used to determine the evolution of flame area and study how the length and velocity scales enhance or diminish flame development. From the perspective of engine performance, it is observed that shorter length scales lead to faster growth of flame kernels. The ratio of kernel diameter to length scale ratio is identified as an independent controlling variable and its effect is studied by varying the initial size of the flame kernel. Smaller ratios result in a faster increase in the flame area. It is also observed that larger velocity scales lead to higher rates of heat release.

Keywords: Flame-kernel; Turbulence-kernel interactions; Premixed turbulent combustion; Flame surface area; Lean methane-air mixtures

*Corresponding author: jabraham@purdue.edu

1. Introduction

Motivated by environmental and energy concerns, there is a growing interest in developing alternative-fueled engines. In this context, natural gas-fueled engines are an attractive alternative to petroleum-fueled engines as it diversifies the energy use and its lower carbon dioxide emissions per unit energy helps to address concerns about climate change [1, 2]. The fuel/air mixture is typically burned lean to lower flame temperature and, hence, reduce nitric oxide emissions. Making the mixture lean also increases thermal efficiency, up to a point [3]. In spark-ignited engines, if the mixture is too lean, igniting the mixture can be a challenge, and misfire and slow combustion rates in the engine can result in a drastic reduction in thermal efficiency. The occurrence of these events is often dependent on the interaction of the flame kernel with the turbulent flow fields, *i.e.*, favorable turbulence conditions can enhance the combustion rates and lead to faster flame speeds while unfavorable conditions can cause quenching of the flame kernels. Hence, it is important to understand the turbulence/kernel interactions in natural gas combustion in lean mixtures, and especially in lean turbulent mixtures, from a fundamental perspective.

The influence of turbulence scales on the turbulence-kernel interactions has traditionally been studied numerically using simple canonical configurations where a counter-rotating vortex pair interacts with a developing flame kernel [4, 5]. These simpler configurations are easier to analyze and the results can be compared with results from experiments conducted with similar configurations [6-8]. The outcome of these interactions has been reported to vary from modest wrinkling of the flame surface to breakup of the connected flame and the formation of distributed flame kernels. In general, the heat release rate has been observed to be enhanced relative to the undisturbed flame, *i.e.*, turbulence enhances flame development. Such studies, however, consider the influence of only one length and one velocity scale at a time. Steinberg and Driscoll [9] studied the dynamical processes of flame surface straining and wrinkling in turbulence-flame interactions in premixed flames using PIV and compared the results with simple flame-vortex configurations. They observed that in the experimental observations, canonical flame-vortex configurations were representative of less than 10% of the turbulence-kernel interaction and even in locations where they were representative of the interactions; they were unable to reproduce the complete evolution of interactions. These differences arise from the fact that during turbulence-kernel interactions, there are multiple scales interacting with the flame at the same time and the

result of these interactions depends on the spectrum of scales. Thus, to understand the influence of turbulence in greater detail and more completely, it is necessary to carry out studies with a realistic turbulent flow-field. In addition to these kernel-vortex studies, there are also several reported studies in the literature which have investigated the interaction of a turbulent flow-field with premixed flames [9-13]. However, these studies typically focus on the interaction of turbulence with planar flames and are conducted at temperatures and pressures not relevant to engines. Since the focus of this study is on interactions of turbulence with developing flame kernels, a discussion of the relevant prior turbulence-kernel interaction studies is provided below.

Kitagawa *et al.* [14] experimentally studied the influence of pressure and Lewis number (Le) on spherically propagating premixed hydrogen–air turbulent flames in a constant volume combustion vessel. They considered equivalence ratios of 0.4-1.0, pressures of 1-5 atm and turbulence intensities of 0.8 and 1.59 m/s. They observed that the ratio of the turbulent flame speed to laminar speed increased with increasing pressure, decreasing equivalence ratio, and increasing turbulence intensity to laminar flame speed ratio. The turbulent flame speed was observed to decrease with increasing Le and they proposed a turbulent flame speed correlation in terms of turbulent Reynolds number (Re) and Le. Liu *et al.* [15] observed a similar correlation between pressure and turbulent flame speed for an equivalence ratio of 0.8 and pressures ranging from 1-10 atm. They attributed this positive correlation to an enhancement in flame surface area due to a hydrodynamic instability induced by the decrease in kinematic viscosity when pressure increases. Fairweather *et al.* [16] studied the influence of hydrogen substitution on spherically-propagating turbulent flame speed in methane-air mixtures. Turbulent flame speed was found to increase with both increased hydrogen content and increased turbulent intensity. With increasing hydrogen addition, lean flames were found to be less sensitive to stretch effects and wider flammability limits were observed.

Klein *et al.* [17] studied the effect of mean curvature of the kernel surface on its propagation using three-dimensional (3-D) DNS with single-step global mechanism in the thin reaction zone regime. They studied the influence of kernel radius on turbulence-kernel interactions. Note that changing the radius changes the initial curvature. They reported that the local flame displacement speed was negatively correlated with the mean curvature of the flames and this correlation was non-linear in nature. It was concluded that there was a minimum kernel size below which the

flame kernel would not be able to sustain flame development. This minimum size was influenced by both diffusion and turbulence conditions.

Dunstan and Jenkins [18] conducted 3-D DNS of turbulence-kernel interactions using a single-step global mechanism for methane to assess the influence of the initial turbulent energy spectrum on the global evolution of the kernel, and the distribution of flame surface density (FSD) in the flame brush. They observed that the global or integrated reaction rates were reduced compared to the rates in a laminar kernel even though the reactions occurred over an increased area. They attributed this to enhanced turbulent heat transfer from the flame by Kolmogorov scale eddies. In a separate study [19], they also studied the effects of hydrogen substitution on turbulent premixed methane–air kernels using a reduced chemistry mechanism at lean equivalence ratios. This study was conducted at 1 bar and considered integral length scales larger than the kernel radius. Higher turbulent flame speeds and greater wrinkling with addition of hydrogen was observed. They compared the turbulent flame speeds for spherically propagating flames with those for planar flames [10] under similar turbulence conditions. The turbulent flame speed enhancement for spherically propagating flames, when compared to planar flames, was higher for hydrogen-enriched flames but was negligible for pure methane flames. This difference in turbulent flame speed enhancement, in the presence of hydrogen substitution, was attributed to non-unity Lewis number effects, and higher strain rates and flame curvature.

The studies discussed above focus on atmospheric or near-atmospheric pressure conditions and low unburned mixture temperatures, and are not relevant to elevated pressure and temperature conditions in engines. Furthermore, such interactions have not been studied for smaller flame kernels which are more susceptible to extinction or for integral length scales which are smaller than the size of the flame kernel. The objective of the present work is to study the influence of a wider range of turbulence scales on flame kernel development in a lean methane-air mixture. This work also characterizes the influence of the ratio of integral length scale to kernel diameter on the outcome of kernel-turbulence interactions. These interactions are studied qualitatively and quantitatively by examining the time evolution of integrated heat release rate, flame area, and turbulent flame speed.

In the section that follows, we discuss the computational setup and conditions employed. A qualitative analysis of turbulence-kernel interactions follows in Section 3. The influence of different turbulence scales on the turbulence-kernel interaction is quantitatively studied in

Section 4. A regime map for the turbulence-kernel interactions is proposed in Section 5. The paper closes with summary and conclusions in Section 6.

2. Computational Setup and Conditions

The numerical code employed in this work [20, 21] solves the conservation equations for multi-component gaseous mixtures with chemical reactions. The spatial discretization is achieved by using a sixth-order compact non-dissipative finite-difference scheme developed by Lele [22] and the resulting tri-diagonal system of equations is solved using the Thomas algorithm. The time integration is achieved through a compact-storage fourth-order Runge–Kutta scheme [23]. At the boundaries, periodic boundary conditions are implemented. In the present work, the mass diffusivities D_k are computed using an effective binary diffusion coefficient model [24]. The code is written in Fortran 90 and parallelized using the message passing interface (MPI). The accuracy of the code has been assessed in several prior studies [5, 21, 25-27].

Figure 1 shows a schematic of the computational setup. The computational domain is two-dimensional (2-D) and measures 5 × 5 mm. The computed laminar flame thickness δ_L estimated with a 5 μm resolution grid is about 50 μm. The computed thickness was estimated by measuring the combined width of the pre-heat and the reaction zone. Hence, the computational domain in terms of flame thickness is 100 δ_L x 100 δ_L. The domain size is selected such that it is 10 times larger than the integral length scale L_I of the flow. A uniform grid with 500 × 500 points, resulting in a resolution of 10 μm, is employed for several of the simulations. Some of the simulations were carried out with 5 μm. Since the flame thickness is 50 μm, it is resolved by 5 points when the resolution is 10 μm. Figure 2 shows transient laminar flame speed development for flames developing from a circular flame kernel when 2, 5, and 10 μm spatial resolutions are employed. The results agree within 10%.

As depicted in Fig. 1, the flame kernel is initialized in the center of the domain with a diameter d_K. The kernel is initialized with a temperature T_b, the temperature of the burned products. The composition of the flame kernel is determined by carrying out an equilibrium simulation of a premixed methane-air mixture. A mass-diffusion layer is initially set up using linear interpolation at the kernel interface. This layer is needed to avoid numerical instabilities

arising from steep gradients in the computational domain in its absence. The width of this layer is l_{th} and it is typically selected to be around 20% of the kernel diameter. Several laminar computations were carried out to study the effect of l_{th} on the flame development and flame propagation in the domain. It was observed that the transients during the flame development period are not affected by l_{th} provided it is in the range of 0-30% of the kernel diameter [28]. If l_{th} is selected to be greater than 30% of the kernel diameter, a longer transient is observed. The steady flame speed is, as expected, not affected by the thickness of the mass diffusion layer.

The domain consists of lean premixed methane-air mixture with an equivalence ratio $\phi = 0.6$. The kinetic mechanism employed in this work is a 21-species 84-reaction reduced mechanism (RM) [29]. The RM has been tested against the 53-species 324-reaction Gri-Mech3.0 detailed mechanism [30] for flame speeds at pressures up to 20 atm and ignition delays at pressures up to 10 atm [29]. Computed laminar flame speeds with the Gri-Mech3.0 and the reduced mechanism (RM) for flames propagating from a flame kernel are shown in Fig. 3. The computations are carried out in the computational domain at pressure and temperature conditions discussed in the following paragraph. The flame speed is estimated by tracking the point of peak chemical heat release along y = 0.0025 m in Fig. 1. An average flame propagation speed is computed at discrete time intervals of 0.02 ms and this is scaled with the ratio of burned and unburned gas densities to obtain the flame speed.

In this work, the unburned methane-air mixture has an equivalence ratio $\phi = 0.6$, temperature of 810 K, and the pressure in the domain of 40 atm. The flame kernel has a diameter $d_K = 500$ μm and temperature $T_b = 2150$ K. The width of the mass-diffusion layer is 100 μm. The laminar flame thickness δ_L and laminar flame speed S_L are estimated to be 50 μm and 0.22 m/s respectively for the given conditions. The simulation employs a CFL number of 0.9 which corresponds to a numerical time step of about 5.78×10^{-9} sec. The computations were carried out on an IBM computing cluster with 48 Intel 64 2.33 GHz dual socket quad core processors. A 10 μm resolution simulation with the RM for 1 ms required 50 days of CPU time.

Turbulence Generation

Like many prior DNS studies, this study is 2-D. In this sense, what is referred to as "turbulence" is not real turbulence, but the compromise in dimension is made to accommodate the more complex kinetics. Recall that 3-D simulations [17, 18] reported in the literature employ

global one-step kinetics which may not capture limit phenomena such as extinction and re-ignition in lean mixtures. In order to study the influence of turbulence scales on turbulence-kernel interactions, it is necessary to initialize the simulation domain with a velocity field that reproduces a specified turbulent spectrum. This can be done by using either experimental measurements of the turbulent velocity field or by generating synthetic turbulence fields. The former is generally not realistic since measurements of the turbulent velocity field at the relevant engine conditions are not readily available. In this work, a stochastic approach based on digital filtering will be utilized to generate initial conditions for the turbulent flow-field [31]. This method generates synthetic turbulence through a linear combination of uncorrelated random white noise fields such that the resulting velocity field has prescribed turbulent length scales and Reynolds stresses.

The basic premise of developing a turbulent flow field using this method is as follows. Any complex flow field can be considered as the linear superposition of multiple simpler flow fields. The goal is to manifest a turbulent flow field with prescribed turbulent length scales and Reynolds stresses. Thus, it is possible to apply the superposition principle and generate separate flow fields which can then be combined. The weight factors of these simpler flow fields are determined from the prescribed length scales and Reynolds stresses. However, there still remains the question of how to generate these simpler flow fields. The simpler flow fields are constructed by first generating white noise fields, i.e. random fields with zero mean, which are un-correlated with each other. A Gaussian filter of variance σ can then be applied to a white noise field to generate a flow field with an autocorrelation function related to the variance. Thus, the resulting flow field has an auto-correlation function similar to the shape of the auto-correlation function of homogenous isotropic turbulence in its final period of decay. This implies that the turbulent spectrum generated by this method is consistent with the viscous nature of the Navier-Stokes equations [32]. The detailed equations for determining the weight factors can be found in Ref. [31]. The velocity vectors of a typical turbulent flow-field, with an integral length scale L_I = 0.5 mm and turbulence intensity u' = 2 m/s, are shown in Fig. 4. This flow field has been used in studying turbulence-kernel interactions for Case 1 in Table 1 in this work.

In this work, this method has been extended for periodic boundary conditions and is used to generate 2-D periodic turbulent flow fields with the prescribed input Reynolds stresses and length scales. The generated flow field is then used as the initial velocity field for the DNS

simulations to study the effect of turbulent length and velocity scales on turbulence-kernel interactions.

Table 1 shows the turbulent length and velocity scales employed in this study. The integral length scale L_I varies from 0.1 mm to 0.5 mm and the turbulence intensities range u' from 0.5 to 4 m/s. The kernel diameter d_K is fixed at 0.5 mm except for Cases 6 and 7 where it is increased to 0.75 mm and 1 mm respectively. The turbulent Reynolds number Re_T varies from 5 to 100 and the Damköhler number Da varies from 0.1 to 1.0. Cases 1-7 are simulated with a 10 μm resolution while Cases 8-10 are simulated with a 5 μm resolution. Since the number of grid points is kept constant, the computational domains for Cases 8-10 have a smaller physical size.

Table 1: Simulation parameters

Case	L_I (mm)	u' (m/s)	L_I/δ_L(μm)	Re_T	Da	d_K (mm)	λ (L_I/d_K)
1	0.1	2.0	2.0	20.5	0.195	0.5	0.2
2	0.15	2.0	3.0	30.8	0.292	0.5	0.3
3	0.2	2.0	4.0	41.0	0.390	0.5	0.4
4	0.4	2.0	8.0	82.1	0.780	0.5	0.8
5	0.5	2.0	10.0	100.0	0.975	0.5	1.0
6	0.15	2.0	3.0	30.8	0.292	0.75	0.2
7	0.2	2.0	4.0	41.0	0.390	1.0	0.2
8	0.1	1.0	2.0	5.13	0.780	0.5	0.2
9	0.1	3.0	2.0	30.8	0.130	0.5	0.2
10	0.1	4.0	2.0	41.0	0.0975	0.5	0.2

In developing flame kernels, the turbulence-kernel interaction is also dependent on an additional length scale ratio which is based on the size of the flame kernel. In Table 1, this length scale ratio is characterized as λ which is defined as the ratio of the integral length scale to the kernel diameter. This parameter is a measure of the number of turbulent eddies interacting with

the flame kernel. Smaller λ values suggest larger number of smaller eddies interacting with the flame kernel. Such interaction is more likely to result in greater surface convolution. Larger λ suggest smaller number of large scale eddies interacting with the flame kernel and thus are more likely to cause "bulk" convection of the flame kernel. In this work, we vary this parameter to study how this length scale ratio can influence the transient evolution of the turbulence-kernel interaction.

3. Qualitative analysis of turbulence-kernel interactions

We will now consider a case where the integral length scale L_I is 0.1 mm, u' is 2 m/s, and d_K = 0.5 mm, i.e. λ = 0.2 (Case 1 in Table 1). Figure 5 shows the temperature contours in the domain at different time instants. The kernel is specified to have an initial circular configuration (Fig. 5a). As the kernel starts to interact with the turbulent flow field, the surface of the kernel starts to wrinkle, see Fig. 5b. L_I is smaller than the kernel diameter, *i.e.* $\lambda < 1$, and as a result multiple eddies interact with the kernel and causes small-scale wrinkling. These surface deformations lead to local thickening due to enhanced local mixing. Strain and curvature effects due to the kernel-turbulence interactions also lead to variations in flame thickness as can be seen in Fig. 5c. If the strain is large, the turbulent eddies can cause local extinction of the flame. Such extinction can be observed in Fig. 5d where a pair of turbulent eddies extinguishes the flame at the location indicated on the figure.

The local extinction leads to the formation of a smaller secondary flame kernel as seen in Fig. 5e. This regime of turbulence/kernel interactions will be referred to as the kernel-breakup regime. The smaller kernels are potential sources of additional flames. Such secondary flame kernels, being smaller in size than the original flame kernel during the early stages of kernel growth are, however, susceptible to extinction because of rapid heat diffusion relative to heat generation. Consequently, flame development from these kernels is at best slower than from the original kernel. In this particular case, the secondary kernel is large enough to sustain flame development, see Figs. 5f and 5g. It can be observed in Fig. 5h that the flames propagating from the secondary kernel eventually merge with flames developed from the initial kernel. We can also identify thin streaks of high temperature regions being formed at several locations. These correspond to small amounts of hot combustion products being transported away from the kernel by the flow field (Figs. 5d and 5f). These regions can also act as potential spots for formation of

new secondary kernels. Another observation is the formation of trapped regions of unburned gas, see Figs. 5g and 5h which is characteristic of a multiply-connected wrinkled flame.

The kernel deformation and subsequent breakup are a consequence of local interactions of the flame with the flow field. Variations in strain and curvature induced in the flame by the flow field can lead to flame weakening and eventual extinction of the flame. It can be observed in Fig. 6 that regions of high positive curvature (flames convex to the unburned gas), e.g. locations identified by the letter B in the figure, are associated with thickened flames while locations of negative curvature, e.g. locations identified by the letter A, are associated with thinner flames. These variations can also be observed in Fig. 5 where variation of temperature as a function of physical distance is plotted across two different cross-sections of the flame identified as A (Fig. 7a) and B (Fig. 7b) on Fig. 6. Comparing the flame thickness in Figs.7a and 7b, it is evident that the convex flames regions are thicker while concave flame regions are thinner. Physically, the correlation between positive curvature and increasing flame thickness can be interpreted as defocusing of heat to a larger volume of unburned gas in regions of positive curvature. This increased heat dissipation brings about a slower rate of reaction and thus leads to thicker flames with slower flame speeds. The correlation has also been numerically explained by Chakraborty *et al.* [13] who first demonstrated that there was negative correlation between tangential strain rates and flame curvature and then argued that for sub-unity Damkohler number *Da*, increasing tangential strain rate leads to decreasing normal strain rates. In the current simulations, the *Da* is less than unity which results in a negative scaling between tangential and normal strain rates. Thus, positive tangential strain rates correlate with negative compressive normal strain rates which decrease flame thickness and vice versa. Since, positive curvatures correlates with negative tangential strain rates, we observe thicker flames in regions of positive curvature.

These flame stretch effects can lead to eventual local flame extinction and lead to kernel breakup as observed in Fig. 5d. Local flame extinction is also observed in Fig. 6 where two surfaces of negative curvature (positive tangential strain) are convected toward each other by the flow field. At the same time, hot combustion products between the two surfaces are convected away. As the interaction progresses, the combination of thin weakened flames resulting from high strain rates and the reduced temperature between the surfaces resulting from the convection of hot products result in excessive heat loss which, in turn, leads to local extinction of the flame.

Results will now be presented from a simulation where the integral length scale is 0.5 mm and velocity scale is 2 m/s (Case 5 in Table 1), i.e. $\lambda = 1$. Figures 8a-d show the evolution of temperature in the computational domain at different time instants. Since $\lambda = 1$, fewer eddies interact with the flame kernel and this interaction results in the convection of the flame kernel in a 'bulk sense'. The wrinkling evident in the early stages in Fig. 5 is not seen here. We will refer to this regime of interaction as the "kernel convection regime". This behavior is evident in Fig. 8d where the initial flame kernel location is represented by the circle. The displacement of the flame kernel from its initial location is less evident in Case 1 (see Fig. 5g). Comparing Cases 1 and 5, it can be inferred that the length scale ratio (λ) of flow length scale (L_I) to kernel diameter (d_K) plays a significant role in determining the initial interaction and can either lead to wrinkling of the kernel surface or convection of the kernel.

It should be noted that as the kernel evolves, its effective diameter becomes larger than the initial turbulent length scale. This increase in diameter decreases λ. This allows multiple eddies to progressively interact with the surface and deform the flame kernel, see Fig. 8c. Eventually, we do observe the tendency for local extinction and formation of multiple kernels in Fig. 8d when the kernel size is nearly twice the turbulent length scale. Thus, it can be concluded that even though we start from a larger initial λ value, kernel development tends to decrease this ratio and we can move from kernel convection to kernel break-up regime. It should also be noted that the two secondary flame kernels formed in Fig. 8d are comparable in size to the original kernel and thus are unlikely to quench. Once the kernel breakup occurs, it is possible that the interaction of the new flame kernels with the turbulent flow-field will again lie in the kernel convection regime and the interaction mechanism described above is repeated.

In addition to the kernel breakup and the kernel convection regime, a third interaction regime exists at smaller λ values and lower intensities when the flow length scales are not large enough to cause bulk convection and the turbulence intensities (and the resulting turbulent strain) are not high enough to cause breakup of the flame kernel. Figures 9a-d show the evolution of temperature in the computational domain for a simulation where $\lambda = 0.2$ and $u' = 1$ m/s (Case 8 in Table 1). Since $\lambda < 1$, multiple eddies interact with the flame kernel initially and lead to the formation of small-scale surface deformations similar to those formed in Case 1. Although similar in nature, these wrinkles have smaller amplitudes due to lower turbulence intensity and are unlikely to cause kernel breakup. It can be seen in Figs. 9b-c that even though there is flame

weakening and kernel deformation, strain rates are not sufficiently high enough to cause local extinction and lead to kernel breakup. Thus, there is a lack of secondary kernel formation in this regime, see Fig. 9d. Since this interaction regime is characterized by formation of multiple wrinkles or deformations of smaller amplitudes on the surface of the flame kernel, it is referred to as a kernel deformation regime.

Results will now be presented from a simulation where the integral length scale is 0.1 mm and velocity scale u' is 4 m/s to study the influence of turbulence intensity u' (Case 10 in Table 1). Notice that Cases 1 and 10 have the same L_I, i.e. the same $\lambda = 1$, but u' in Case 10 is twice that in Case 1. A grid resolution of 5 μm, as opposed to 10 μm in Case 1, is employed for this case in order to resolve the smaller flow length scales. Figure 10 shows the evolution of temperature in the domain at different time instants. This figure can be qualitatively compared with Fig. 5. It can be seen in Fig. 10a that a wrinkled kernel surface is formed as in Fig. 5b. Note that Figs. 10a and 5b are the same time after start of computation. It can be seen, however, the amplitude of the wrinkling in Fig. 10b is greater than in Fig. 5b. The larger amplitude of wrinkling leads to local extinction at multiple spots in Figs. 10b and 10c where we can observe multiple secondary flame kernels being formed compared to a single secondary formed in Case 1 (see Fig. 5e). These differences are likely to be significant in determining heat release rates. Locally, the local flame-turbulence interactions are similar, in a qualitative sense, for Cases 1 and 10, *i.e.* we observe extinction, similar thickening and thinning of flame in regions of positive and negative curvature. All effects are, however, accentuated in Case 10 relative to Case 1. It should be noted that this may only hold true for moderate intensities and it is possible that at very low and high intensities, the interactions may lead to laminar-like flame propagation or global quenching, respectively.

The cases discussed above were also repeated with global single-step chemistry where the pre-exponential factor and the activation energy were selected to be 3.5 x 10^{11} cm-mol-s units and 100,000 J/mol, respectively. Figure 11 shows the temperature contours in the domain at t = 0.3 ms for RM and the single-step mechanism for a case where L_I is 100 μm and u' is 1 m/s (Case 8 in Table 1). It can be seen by comparing the two figures that the two sets of computations are in good qualitative agreement. In addition, quantitative agreement within 20% was also observed for total heat release rates in the computational domain. This agreement

between the two mechanisms suggests that thermal transport effects rather than detailed chemical effects may control the outcome of turbulence/kernel interactions.

4. Quantitative analysis of turbulence-kernel interactions

We have seen in Figs. 6 and 7 that variations in the flame thickness are evident across the surface of the flame kernel during turbulence-kernel interactions. This variation is attributed to differences in strain and curvature experienced by the flame. The influence of these two parameters on the flame thickness is now studied in greater detail by estimating the flame surface density. Flame surface density is defined as flame surface area per unit volume and is estimated by calculating the gradient of the progress variable c [33], *i.e.*

$$\Sigma = \left\langle \left| \nabla c \right|_{c=c^*} \right\rangle P(c), \tag{1}$$

where $P(c)$ is the probability of finding c in the vicinity of c^*. In our work, we have used a window of $\Delta c = \pm 0.02$ around $c^* = 0.7$ to extract this flame isocontour. The iso-contours of c are closer in thin flames and farther away in thick flames. Since the flame surface density (Σ) is defined as the gradient of c, Σ can be considered as a measure of inverse of flame thickness, *i.e.* increasing Σ is accompanied by decreasing flame thickness and vice versa. Thus, by understanding the influence of strain and curvature on Σ, it is possible to understand their influence on the flame thickness.

The local flame curvature κ can be defined as

$$\kappa = \frac{1}{2} \frac{\partial N_i}{\partial x_i}\bigg|_{c=c^*}, \tag{2}$$

where N_i is local flame normal vector which in turn is defined as

$$N_i = -\frac{1}{|\nabla c|} \frac{\partial c}{\partial x_i}\bigg|_{c=c^*}. \tag{3}$$

These two quantities are also calculated by using a window of $\Delta c = \pm 0.02$ around $c^* = 0.7$ to extract the values at the flame isocontour. The sign convention for this definition is that the flame normal vector is pointed from the products to the reactants and consequently, curvature is positive when the flame has a convex shape when viewed from the reactants. Similar to curvature, a tangential strain rate a_T can be defined as

$$a_T = \left(\delta_{ij} - N_i N_j\right)\frac{\partial u_i}{\partial x_j}\bigg|_{c=c^*} . \quad (4)$$

Strain and curvature are normalized by using laminar flame thickness δ_L and laminar flame speed S_L as scaling parameters. The non-dimensional (normalized) curvature κ_n and strain a_{Tn} are given by

$$\kappa_n = \kappa\delta_L , \quad \text{and} \quad (5)$$

$$a_{Tn} = a_T \frac{\delta_L}{s_L} . \quad (6)$$

Figure 12 shows the variation of Σ with strain rate for Cases 5, 8, and 10. This figure is obtained by first determining the mean flame surface density expected within a certain band of strain rate and then plotting this mean flame surface density variation with strain rate. It is observed that strain and Σ are positively correlated at all times in the three turbulence-kernel interaction regimes. This is in agreement with prior results [13]. The positive correlation has been explained by Chakraborty and Cant [13] who argued that for sub-unity Damköhler number Da, $a_N \sim -a_T$ *i.e.*, increasing tangential strain rate leads to decreasing normal strain rates. In the current simulations, Da is less than unity which results in a strong negative scaling between tangential and normal strain rates. Thus, positive tangential strain rates correlate with negative compressive normal strain rates which decrease flame thickness or increase flame area and vice versa. Figure 13 shows the correlation of curvature and Σ for the three interaction regimes. It is observed that the curvature and Σ are negatively correlated, in agreement with prior results [13]. Physically, this correlation between positive curvature and increasing flame thickness can be interpreted as defocusing of heat to a larger volume of unburned gas in regions of positive curvature. This increased heat diffusion slows the rate of reaction leading to thicker flames with slower flame speeds.

The influence of strain and curvature on the local flame characteristics is further investigated by studying their influence of the local flame speed. This is done by firstly determining the displacement speed of an iso-contour of $c = c^*$ within the flame by the following expressions [34]:

$$S_d = \left[\frac{1}{\rho|\nabla c|}\mathbf{n}.\nabla\left(\rho D\mathbf{n}.\nabla c\right) - 2D\kappa + \frac{\dot{\omega}_c}{\rho|\nabla c|}\right]_{c=c^*} , \quad (7)$$

$$S_1 = \frac{\dot{\omega}}{\rho|\nabla c|}, \tag{8}$$

$$S_2 = \frac{1}{\rho|\nabla c|}\mathbf{n}.\nabla\left(\rho D\mathbf{n}.\nabla c\right) \tag{9}$$

$$S_3 = -2D\kappa. \tag{10}$$

In these equations, the displacement speed is broken down into three components S_1, S_2, and S_3. The effective local flame speed S_d^* can then be obtained from the displacement speed with a density scaling, *i.e.*

$$S_d^* = \frac{\rho^*}{\rho_u} S_d, \tag{11}$$

where ρ^* is the density at the $c = c^*$ iso-contour and ρ_u is the unburned gas density.

Figure 14 shows the variation of flame speed with the tangential strain rate for the three different interaction regimes at a statistically steady time instant. It is observed that the displacement speed of the flame correlates positively with the tangential strain rate which is agreement with prior results reported in the literature [13]. This dependence can be understood by analyzing the response of the three components of the displacement speed in Eq. (7) to the strain rate where S_3 correlates positively with strain rate while the sum of S_1 and S_2 speeds correlates negatively with the strain rate near the product side. The effect of S_3 is found to dominate the other effect and thus a positive correlation is observed.

Figure 15 shows the variation of the flame speed with curvature for the three turbulence/kernel interaction regimes once the flame is fully developed. It can be observed in the figure that curvature and flame speed are negatively correlated. This observation is in agreement with results reported in the literature [13]. Physically, this dependence can be explained on the basis of increased heat diffusion from the flame to the larger volume of the unburned gas in regions of positive curvature. This leads to diffuse flame regions and decreases the speed of the flame. On the other hand, in regions of negative curvature, there is focusing of the heat transfer from the flame kernel to the unburned gas which increases the speed of the flame. This correlation can also be explained mathematically using the different displacement speed components in Eq. (10) where it is observed that the sum of S_1 and S_2 speeds correlate positively with curvature near the product gas. However, S_3 correlates negatively with curvature and this

effect dominates the other components leading to a net negative correlation between curvature and the displacement speed. We would like to note that the correlations of flame speed and flame surface density with strain and curvature that we identify at elevated pressures and temperatures show the same qualitative trends as those reported in literature for atmospheric conditions [13]. This suggests that pressure and temperature effects are not very significant during turbulence-kernel interactions.

It can be observed in Figs. 12-15 that the mean values of local flame parameters such as flame surface density and flame speed are primarily dependent on the local values of the strain and curvature and not significantly influenced by the regime of interaction. This observation is not surprising as the physical processes during flame propagation are influenced by strain and curvature. Of course, the range of strain rates and curvatures encountered by the kernel will vary depending on the interaction regimes. Figure 16 shows the probability density function (*pdf*) of strain rate for Cases 5, 8, and 10. The strain rate *pdfs* are found to have a Gaussian shape which is not surprising due to the stochastic nature of the turbulent flow field. This is in agreement with observations in prior work [35]. It can be seen in the figure that as we decrease integral length scale and increase turbulence intensity, the width of the *pdf* increases and the flame is influenced by higher strain rates. The range of strain rates encountered by the flame is greatest in Case 10 which lies in the breakup regime. The normalized extinction rate for a planar flame under simulated conditions was found to be approximately 6 from laminar counter-flow premixed flame simulations. It can be seen in Fig. 12 that the peak strain rates observed in Case 10 are higher than this extinction strain rate and thus local extinction is expected. This expectation is in agreement with Figs. 10a-d where significant flame extinction and kernel breakup are observed. On the other hand, the peak strain rates are considerably lower than the extinction strain rate in the kernel convection (Case 5) and kernel deformation regimes (Case 8). Consequently no local extinction is observed in Figs. 8 and 9.

A similar analysis of the curvature *pdf* is carried out by plotting the fully developed curvature *pdfs* for the three interaction regimes in Fig. 17. The curvature *pdfs* are also Gaussian in shape and both positive and negative curvatures are likely to be encountered. The *pdfs* are biased towards the positive side since the initial flame kernel has a positive curvature. It can be seen in Fig. 17 that the range of curvatures encountered in turbulence-kernel interactions is dependent mainly on the integral length scale and it is not a strong function of the turbulence

intensity. Since a larger curvature value correlates with a smaller radius of curvature of the flame surface, it is expected that smaller integral scales, *i.e.* smaller λ values, would lead to small scale wrinkling of the kernel surface. This can be in Figs. 9 and 10 where λ is 0.2 and small scale wrinkling of the flame kernel is evident. This small scale wrinkling is absent at larger λ values as can be seen in Fig. 8 for a case where λ is 1.

The discussion above has focused on the local flame statistics during turbulence-kernel interactions. Since our interest also lies in studying the role of turbulent flow scales on flame development and kernel growth, we will now quantitatively characterize the influence of length and velocity scales on global parameters during turbulence-kernel interactions. In order to study these effects, six additional simulations were carried out by varying L_I, u' and d_K. These cases are listed in Table 1. We will now evaluate the results by considering the evolution of flame area for the different cases. Recall that the flame surface density Σ quantifies the surface area of the flame per unit volume. The flame surface area in any computational cell can be computed by multiplying the net Σ at any given time instant by the volume of that cell. Figure 18 shows the time evolution of the non-dimensional flame area, *i.e.* instantaneous area/initial area, in the domain for five length scales (Cases 1-5). All simulation parameters apart from the L_I (and λ) are kept constant. It can be observed from the figure that decreasing L_I increases the growth rate of flame area. As L_I is decreased, larger number of eddies can interact with the flame kernel which leads to significant wrinkling of the flame kernel and faster increase in the surface area of the flame kernel. This is evident in Fig. 17 where smaller length scales generate a wider range of curvatures and lead to small scale wrinkling of the kernel surface. On the other hand, increasing L_I promotes bulk convection of the kernel and slower surface deformation. The increasing growth rate of the flame increases the heat release rates.

The *THRR* is computed as the sum over all the computational cells of the heat release rate *HRR* in each cell, where *HRR* is defined as

$$HRR = \sum_{i=1}^{N} \dot{w}_i h_i^0 , \tag{12}$$

where $\dot{w}_i$ is the production/destruction rate of species i, h_i^0 is the enthalpy of formation of species i, and N is the total number of species. *THRR* is dependent on the flame surface area and the speed of the reaction front. If the flame is highly strained, it can weaken and reduce the

surface area of the flame which decreases the *THRR*. Thus, this quantity can provide a quantitative measure of the extent to which combustion is accelerated or decelerated during the interaction.

Figure 19 shows the variation of total heat release rate (*THRR*) inside the simulation domain with time. Comparing Figs. 18 and 19, it can be observed that the initial differences between the different cases are much smaller in *THRR* when compared to the flame area. It is possible that the area may increase rapidly but the reaction rates may slow down because of strain effects and flame weakening. This can explain the difference. As evidence of this, Fig. 16 shows that for a fixed intensity as length scale is decreased, the range of strain rates that is encountered by the flame increases.

It would be interesting to examine the results in non-dimensional time, recognizing that the turbulent time scales change as L_I is changed. Note, however, that it is the physical time which is relevant for practical applications in engines where there is a finite time available for combustion of the charge. Eddy turn over time is defined as the ratio of L_I to u'. For the current cases, the eddy turn-over time varies from 0.05 ms for the smallest length scale (Case 1) to 0.25 ms for the longest (Case 5). Figure 20 shows the transient evolution of the non-dimensional flame area in the domain for the five length scales. The time axis for this figure has been non-dimensionalized by the eddy turn-over time for the different cases. It can be observed that a larger L_I leads to a faster growth in non-dimensional time, i.e. the trends from Fig. 18 reverse. The trends of Fig. 20 are consistent with conclusions drawn from flame-vortex interaction studies [35], and these trends have been explained by the increase in Re_T as L_I is increased. We may reason that in the same eddy turn-over time, the extent of interaction between the turbulence and kernel may be about the same and since u' are same, the growth rate of area may be about the same. Two factors counteract this, however. Firstly, there is local extinction and the flame is strained to a greater extent for smaller length scales. This decreases the effective flame area in a given eddy turn-over time. Secondly, as mentioned before, there is a finite transient flame development period. The non-dimensional time scale does not account for the fact that the transient flame development between different length scales occur in different eddy turn-over times. These two factors coupled together lead to differences in the growth rates.

In the simulations discussed above, the kernel diameter is kept constant while L_I is varied. The differences in interactions arise from the interaction of a different number of eddies with the flame kernel at a given time instant. It is possible that the governing parameter for turbulence-kernel interaction is the length scale ratio λ of turbulent length scale to kernel diameter as this ratio ensures that the number of eddies interacting with the flame kernel is constant. This possibility is investigated by comparing three simulations with a constant $\lambda = 0.2$ (Cases 1, 6 and 7 in Table 1). Figure 21 shows the transient evolution of the non-dimensional flame area for these three cases. It is observed that the growth rate in flame area for these three cases is about the same. The *THRR* profiles for these cases also show similar trends suggesting that it is the numerical transient development which is primarily responsible for the differences in the early stages of flame development in Figs. 18 and 19. A similar set of simulations was also carried out at $\lambda = 0.4$ and the same conclusions were drawn.

It can be inferred from the results of Fig. 21 that an important governing parameter for turbulence kernel interaction is the ratio of the flow length scale to kernel diameter λ as it determines the number of eddies which can interact with a given flame kernel which, in turn, is responsible for the extent of wrinkling of the flame kernel. However, this length scale ratio λ is only meaningful as long the thermal diffusion length is much smaller than the kernel diameter. When the kernel diameter becomes comparable to the thermal diffusion length, the flame kernel starts to quench initially which delays the onset of flame propagation. The extension of the transient flame development period brings a significant difference in the initial growth rate of flame area. However, once the transient flame development period is over, the growth rate for the smaller kernels are also similar to larger flame kernels with the same λ. This influence was assessed by considering the same L_I but different d_K. The effect can be observed in Fig. 22 where the smaller kernel grows at a smaller rate due to larger diffusive loses during the initial flame development. However, once the initial flame development period is over, both the kernels grow at similar rates.

Results will now be presented to examine the influence of u' on turbulence-kernel interactions. For this set of simulations, all parameters apart from u' are kept constant and transient evolution of *THRR* is tracked. Figure 23 shows the transient evolution of the *THRR* for four cases (Cases 1, 8, 9 and 10 of Table 1). The figure shows that during the initial period (before 0.3 ms), lower u' shows greater *THRR*. This observation is in agreement with the findings

of Dunstan and Jenkins [19] who observed lower global reaction rates for higher turbulence intensities in the early kernel development period. Beyond this initial period, the higher u' results in greater *THRR*. This difference in behavior between the early and subsequent time periods can be explained as follows. It can be seen in Fig. 16 that higher turbulence intensity leads to greater strain rates which leads, in turn, to local extinction of the flame. This can result in lower total heat release rates. At the same time, it also leads to greater flame wrinkling which leads, in turn, to a larger flame area. This results in greater total heat release rates. Thus, increasing u' has two competing effects on the total heat release. During the early flame development period, it is likely that the local extinction phenomena dominates and we observe lower *THRR* for higher u'. However, past the early flame development period, the higher amplitude of wrinkling and larger flame areas associated with higher u' dominate the local extinction phenomena and higher u' leads to greater *THRR*.

We would like to note at this point that, like many prior DNS studies, our study is two-dimensional in nature. In this sense, what is referred to as "turbulence" is not real turbulence, but the compromise in dimension is made to accommodate the more complex kinetics in order to resolve limit phenomena such extinction and re-ignition. The loss dimensionality of the computations is likely to result in quantitative differences between 2D and 3D computations [36, 37]. Nonetheless, we have observed good qualitative agreement for the correlations between strain rates, curvature, flame displacement speed, and flame surface density statistics between our 2D computations (see Figs. 12-17) and those reported in the literature [13]. This agreement suggests that, despite the expected quantitative differences between 2D and 3D computations, qualitative conclusions drawn from the 2D computations such as the trends for the dependence of flame surface area and total heat release rate variation with different turbulent scales, and the observed interaction regimes are still valid.

5. Regime Map

In prior work, turbulence-flame interactions have been characterized using non-dimensional parameters based on L_I and u'. Peters [33] suggested a regime map based on the ratio of L_I to laminar flame thickness and u' to laminar flame speed (see Fig. 2.8 of Ref. [33]). In addition to these parameters, Re_T the turbulent Reynolds number, and Ka_L the Karlovitz number, defined as

the square of laminar flame thickness to Kolmogorov length scale, are controlling parameters. When $Ka_L < 1$, i.e. the laminar flame thickness is smaller than the Kolmogorov length scale, the flame retains its laminar flame structure and a flamelet regime is observed. The flamelet regime itself can be subdivided into wrinkled or corrugated flamelets depending on the turbulence intensity of the flow field. When $Ka_L > 1$, the turbulence-flame interactions lie in the reaction sheet regime if the Kolmogorov length scale L_K is larger than the reaction layer thickness. In this regime, the pre-heat zone of the flame structure is affected which leads to flame broadening. If L_K is smaller than the reaction layer thickness, the entire flow behaves as a well-stirred reactor.

In turbulence-kernel interactions, the interaction is also dependent on the size of the flame kernel. We have observed in our work that the additional length scale ratio λ, defined as the integral length scale to the kernel diameter ratio, is important in determining the nature of the interaction and the transient development of the flame kernel. It is possible to describe the different turbulence-kernel interactions observed in this work by drawing a regime map using λ and u'/s_L as axes (see Fig. 24). This regime is developed by conducting 11 more computations in addition to the 10 cases listed in Table 1. The (u', λ) parameter combinations for this set of computations include (1, 5), (2, 5), (4, 5), (1, 1), (4, 1), (0.5, 0.2), (1, 0.4), (0.5, 0.4), and (0.5, 0.6). The first 5 cases listed above lie in the kernel convection regime while the last 4 lie in the kernel wrinkling regime. Two additional cases with (0.1, 0.2) and (0.1, 1) were also simulated during the last revision to observe the laminar flame regime. Thus, we have 8 cases lying in the kernel breakup regime, 6 cases lying in the kernel convection regime, and 5 cases lying in the kernel wrinkling regime. In Fig. 24, as we increase the length scale, we move horizontally away from origin since λ increases. Increasing turbulence intensity corresponds to moving vertically downwards. Based on the different length scale ratios, this regime map can be divided into 3 broad interaction zones.

Kernel breakup regime is observed for $\lambda < 1$ with moderate to high turbulence intensities ($u'/s_L > 5$). Smaller λ values allow for larger number of eddies to initially interact with the flame kernel which leads to larger number of small-scale surface deformations on the surface of the flame kernel. In this regime, flame broadening is more evident and pre-heat zone of the flame structure is significantly affected. We also observe local extinction of the flame kernel which can lead to formation of one or more secondary flame kernels. In this regime, local extinction and flame weakening can lead to slower kernel growth rates in the initial flame development period.

However, once the initial transient is past, large number of surface deformations coupled with multiple flame kernels lead to faster kernel growth.

Kernel deformation regime is observed for small λ values with low turbulence intensities (u'/s_L <5). In this turbulence-kernel interaction, we observe small scale deformations similar to those in the kernel breakup regime. However, the amplitudes of these deformations are smaller and the low intensity turbulent eddies are unable to cause local extinction or kernel breakup. The primary kernel growth acceleration mechanism is small scale surface deformation and the absence of secondary flame kernels lead to slower growth rates compared to the breakup regime.

Kernel convection regime is observed for large λ values which are typically of the order of 1 or larger. Due to large λ values, turbulent eddies are comparable or larger than the kernel diameter and fewer eddies can interact with the flame kernel. This interaction is characterized by bulk convection and large-scale deformation of the flame kernel and there is a general lack of local extinction in the flame kernel. The kernel growth is dominated by the convection process and this leads to a slower kernel growth rate compared to the breakup and the deformation regimes.

It should be noted that the turbulence-kernel interaction does not necessarily lie in a single regime during the kernel evolution. This is a consequence of the fact that λ does not stay constant and tends to decrease as the kernel grows. This leads to a horizontal movement from the kernel convection regime to the kernel break-up regime on the regime map which is represented by a horizontal arrow in Fig. 24. Thus, kernel convection is likely to be followed by either breakup or kernel deformation, provided the interaction is allowed to proceed for a long enough time. Two additional computations (to those reported earlier) where u' is fixed at 2 m/s but λ is 1.5 for one case and $\lambda = 5$ for the second case were carried out. It was observed that the time required for the interaction to reach the break-up regime is dependent on the initial λ value and increases with increasing λ values.

6. Summary and Conclusions

In this work, we investigate the influence of turbulence length and velocity scales on a flame-developing from a kernel in a lean methane-air mixture. The conditions considered are relevant

to spark ignition of lean mixtures in homogeneous-charge natural-gas-fueled reciprocating engines. It is shown that a length scale ratio λ defined as the ratio of turbulent length scale L_I to kernel diameter d_k ratio is one of the governing non-dimensional parameters responsible for determining the outcome of turbulence-kernel interactions. In engines, d_k is dependent on the method of ignition. For example, in spark-ignited engines, d_k can be correlated with the spark plug gap width. In hot-gas jet ignited engines, the parameter is dependent on the orifice diameter and initial turbulent length scales. Hence, the conclusions of this work can be related to practical engine behavior.

Three distinct interaction regimes are observed for different values of the ratio λ of the turbulent length scale L_I to the initial kernel diameter d_k. A kernel breakup regime is observed for smaller λ and higher u'. In this regime, the surface of the flame kernel is highly wrinkled. Thicker flames are observed in region of positive curvature and thinner flames are observed in regions of negative curvature. High strain rates also cause local extinction and lead to formation of secondary kernels. The amplitude of the wrinkles and the number of secondary flame kernels increases with increasing u'. These secondary kernels tend to cause flame propagation and eventually merge with the primary flame kernel to form either singly-connected or multiply-connected flames. A kernel deformation regime is observed for small λ values with low turbulence intensities where small scale deformations, similar to those in the kernel breakup regime, are observed. However, the amplitudes of these deformations are smaller and the low intensity turbulent eddies are unable to cause local extinction or kernel breakup. A kernel convection regime is observed for larger λ where the flame kernel is convected along with the flow and lesser amount of surface deformation is observed. Kernel breakup is observed once the size of the burned region grows past the size of the turbulent length scale. Secondary kernels formed are of comparable size and do not have a tendency to quench unlike the secondary flame kernels in the wrinkling regime. The outcome of turbulence-kernel interactions identified in this work is presented in a regime map. The non-dimensional parameters used to generate this regime map are the length scale ratio λ and the velocity scale ratio u'/s_L. From a practical engine perspective, the kernel deformation regime would appear to be the most suitable for engines because it leads to greater heat release rates and is less likely to lead to cycle-to-cycle variability. On the other hand, in the convection regime, the kernel is likely to be advected to different parts

of the chamber during the kernel development period and this can result in greater cycle-to-cycle variability.

Flame surface area and *THRR* are estimated in order to quantify the influence of turbulent scales on turbulence-kernel interactions. It is observed that both *THRR* and flame area increase faster for smaller L_I in physical time. This is attributed to greater flame surface area due to greater wrinkling when turbulent length scales are shorter. These trends reverse in non-dimensional time (scaled with eddy turn-over time) reflecting the influence of local extinction when length scales are shorter and a smaller contribution of slower kernel time period during the flame development transients for longer length scales. The influence of u' on *THRR* is also studied and the influence is not monotonic in time. Higher turbulence intensities lead to greater local extinction and flame wrinkling, and lower THRR, in the early phase but THRR increases beyond the initial transient period when flame wrinkling effects dominate.

Acknowledgements

The authors thank the National Center for Supercomputing Applications (NCSA) for providing the computing resources employed for this work. Financial support for this work was provided by Caterpillar Inc.

References

[1] Natural gas overview, *http://www.natural gas.org/*

[2] U.S. Department of Energy. *International Energy Outlook*. Technical Report DOE/EIA - 0484, U.S. Department of Energy, September 2008.

[3] J.B. Heywood, *Internal Combustion Engine Fundamentals,* McGraw-Hill Inc. (1988), New York, NY.

[4] T. Echekki, H.K. Gokula, *Phys. Fluids* 19 (2007) 043604.

[5] H. Reddy, J. Abraham, *Combust. Flame* 158 (2011) 401-415.

[6] D.A. Eichenberger, W.L. Roberts, *Combust. Flame* 118 (1999) 469–478.

[7] Y. Xiong, W.L. Roberts, M.C. Drake, T.D. Fansler, *Combust. Flame* 126 (2001) 1827–1844.

[8] Y. Xiong, W.L. Roberts, *Proc. Combust. Inst.* 118 (1999) 469.

[9] A.M. Steinberg, J.F. Driscoll, *Combust. Flame* 156 (2009) 2285–2306.

[10] E.R. Hawkes, J.H. Chen, *Combust. Flame* 138 (2004) 242–258.

[11] N. Chakraborty, R.S. Cant, *Phys Fluids* 17 (2005) 065108.

[12] E.R. Hawkes, J.H. Chen, *Combust. Flame* 144 (2006) 112-125.

[13] N. Chakraborty, E.R. Hawkes, J.H. Chen, R.S. Cant, *Combust. Flame* 154 (2008) 259–280.

[14] T. Kitagawa, T. Nakahara, K. Maruyama, K. Kado, A. Hayakawa, S. Kobayashi, *Intl. J. Hydrogen Energy* 33 (2008) 5842-5849.

[15] C.C. Liu, S.S. Shy, H.C. Chen, M.W.Peng, *Proc. Combust. Inst*. 33 (2011) 1293–1299

[16] M. Fairweather, M. Ormsby, C. Sheppard, R. Woolley, *Combust. Flame* 156 (2009) 780–790.

[17] M. Klein, N. Chakraborty, K.W.Jenkins, R.S. Cant, *Phys. Fluids* 18 (2006) 055102.

[18] T.D. Dunstan, K. Jenkins, *Proc. Combust. Inst*. 32 (2009) 1427–1434.

[19] T.D. Dunstan, K.W. Jenkins, *Intl. J. Hydrogen Energy* 34 (2009) 8389-8404.

[20] J. Abraham, V. Magi, *Int. J. Computational Fluid Dynamics* 8 (2007) 147-151.

[21] A. Viggiano, V. Magi, *Combust. Flame* 137 (2004) 432-443.

[22] S.K. Lele, *J. Comput. Phys.* 103 (1992) 16-42.

[23] B. Carnahan, *Applied Numerical Models*, John Wiley & Sons, New York, 1969, p. 363.

[24] R.B. Bird, W.E. Stewart, E.N. Lightfoot, *Transport Phenomena*, Wiley (1960), New York.

[25] J.W. Anders, V. Magi, J. Abraham, *Computers and Fluids* 36 (2007) 1609-1620.

[26] J.W. Anders, *Turbulence and Residual Gas Effects in Pulsed Diesel Jets*, PhD. Thesis, Purdue University, August 2006.

[27] R. Venugopal, J. Abraham, *Combustion and Flame* 153 (2008) 442-464.

[28] H. Reddy, J. Abraham, *Fuels* 89 (2010) 3262-3271.

[29] A. Kazakov, M. Frenklach, http://www.me. berkeley.edu/drm/

[30] G.P. Smith, D.M. Golden, M. Frenklach, N.W. Moriarty, B. Eiteneer, M. Goldenberg, C.T. Bowman, R.K. Hanson, S. Song, W.C. Gardiner Jr., V.V. Lissianski, Z. Qin , http://www.me. berkeley.edu /gri_mech/

[31] M. Fathali, M. Klein, T. Broeckhoven, C. Lacor, M. Baelmans, *Intl. J. of Numerical Methods in Fluids,* 57 (2007) 93-117.

[32] G.K. Batchelor, *The Theory of Homogeneous Turbulence*, Cambridge University Press (1954), Cambridge, UK.

[33] N. Peters, *Turbulent Combustion*, Cambridge University Press (2000), UK.

[34] T. Echekki, J.H. Chen, *Combust. Flame* 106 (1996) 184-202.

[35] C. Meneveau, T. Poinsot, *Combust. Flame* 86 (1991) 311-332.

[36] S. Gashi, J. Hult, K.W. Jenkins, N. Chakraborty, S. Cant, C.F. Kaminski, *Proc. Combust. Inst.* 30 (2005) 809-817.

[37] D. Thévenin, O. Gicquel, J. De Charentenay, R. Hilbert, D. Veynante, *Proc. Combust. Inst.* 29 (2002) 2031-2039.

Figure(s)

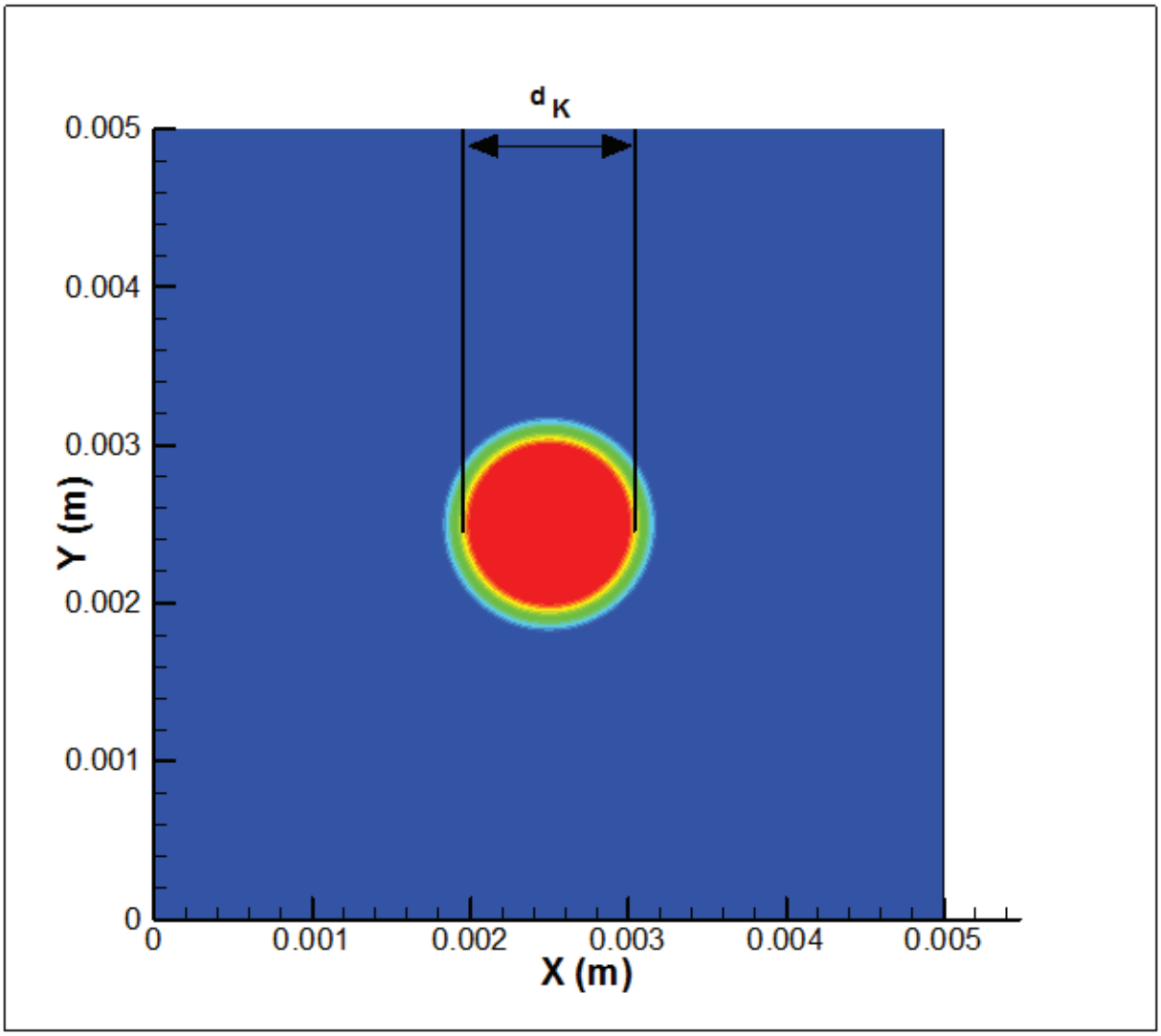

Fig. 1: Schematic of the problem setup.

Figure(s)

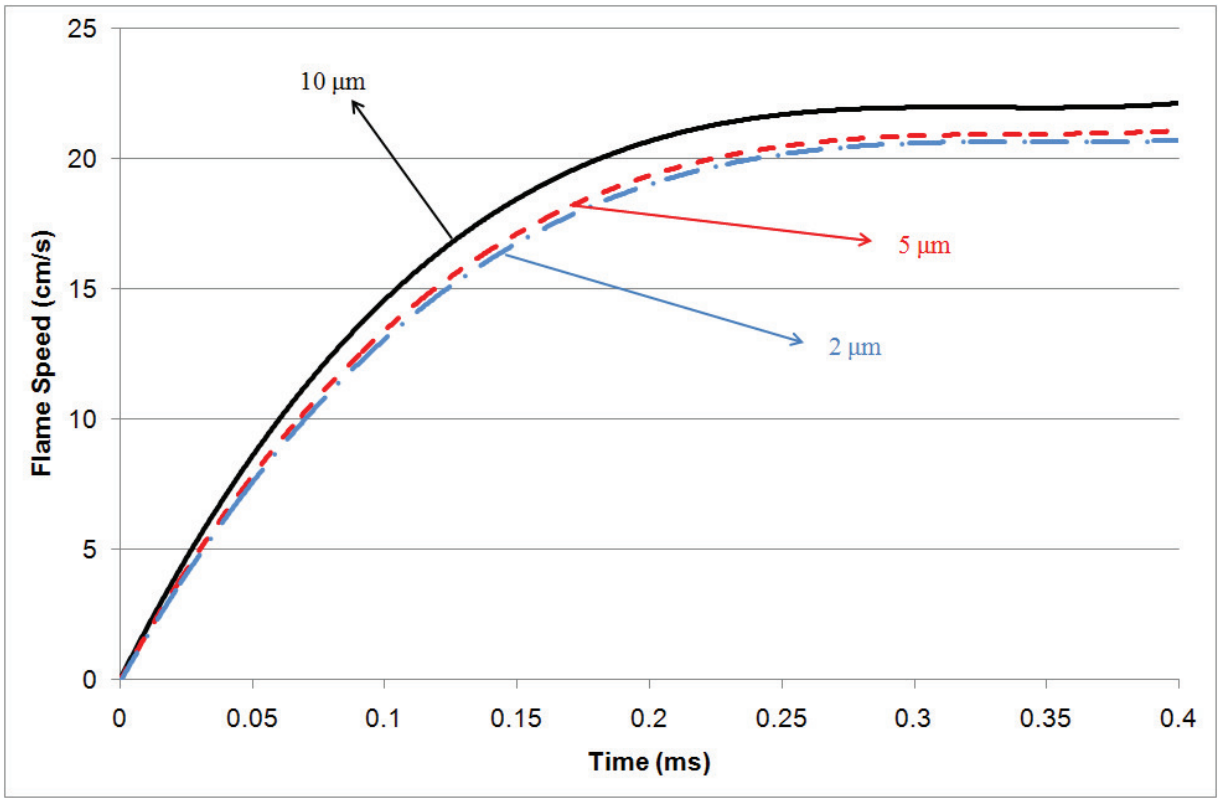

Fig. 2: Time evolution of laminar flame propagation speed with different grid resolutions for a simulation with $T_b = 2150$ K and $d_K = 500$ µm.

Figure(s)

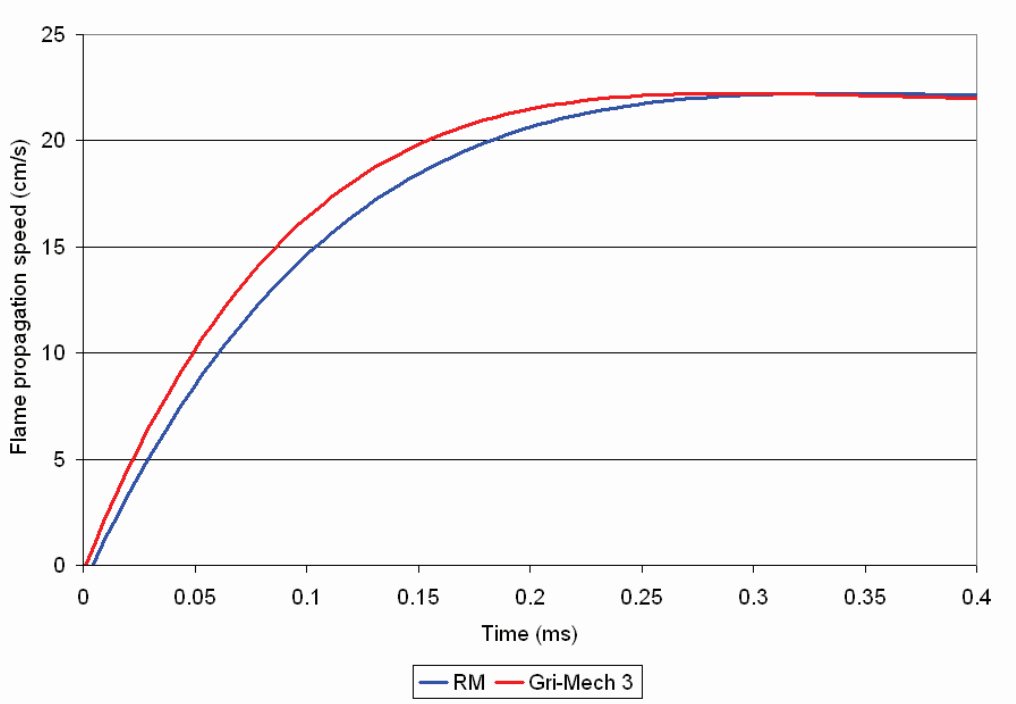

Fig. 3: Time evolution of laminar flame propagation speed with a reduced (RM) and detailed (Gri-Mech3) chemical mechanisms for a simulation with $T_b = 2150$ K and $d_K = 500$ µm.

Figure(s)

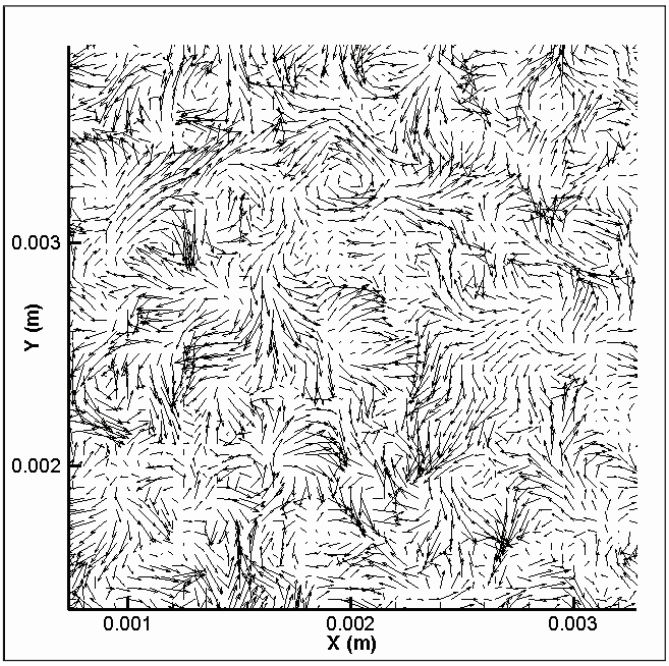

Fig. 4: Velocity vectors of a typical turbulent flow field for a case with L_I = 0.1 mm and u' = 2 m/s.

Figure(s)

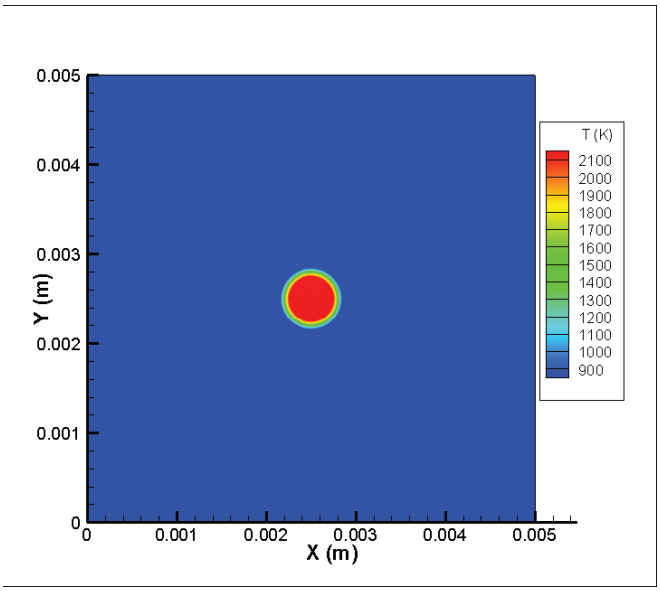

(a)

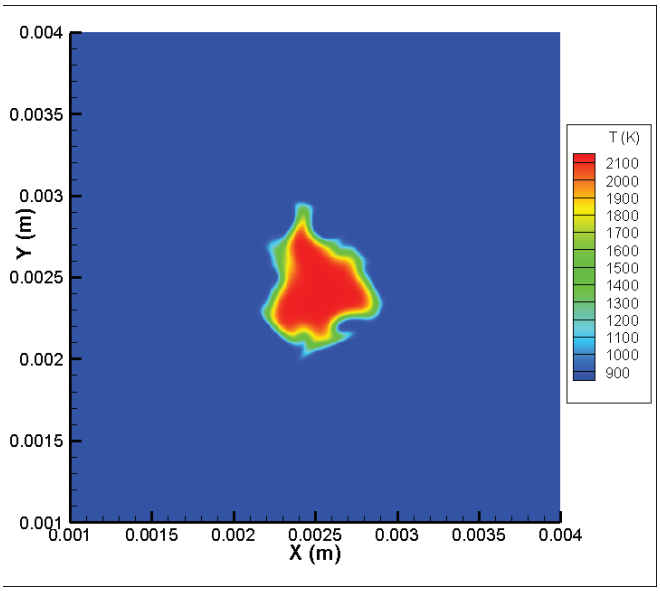

(b)

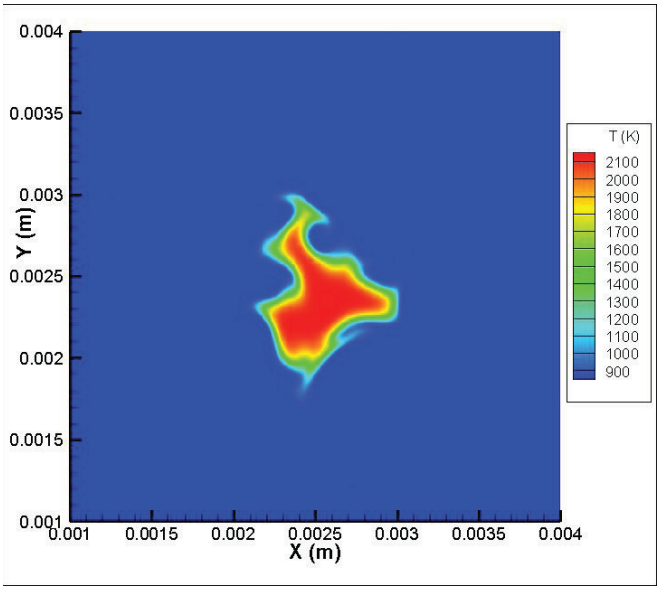

(c)

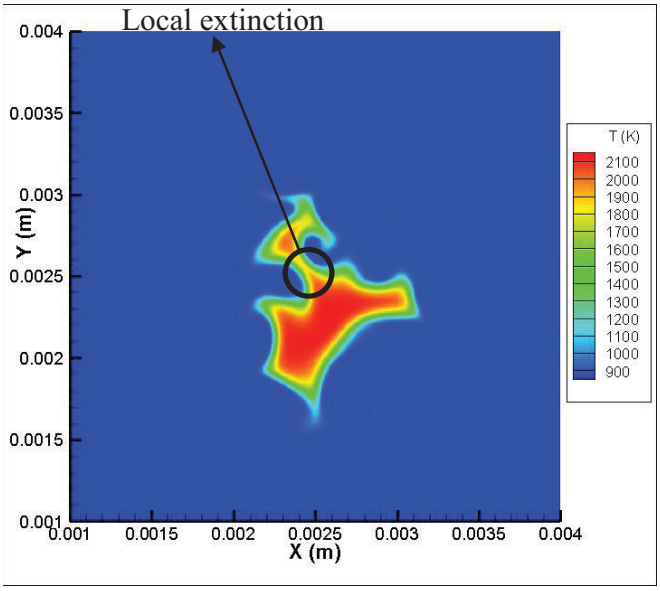

(d)

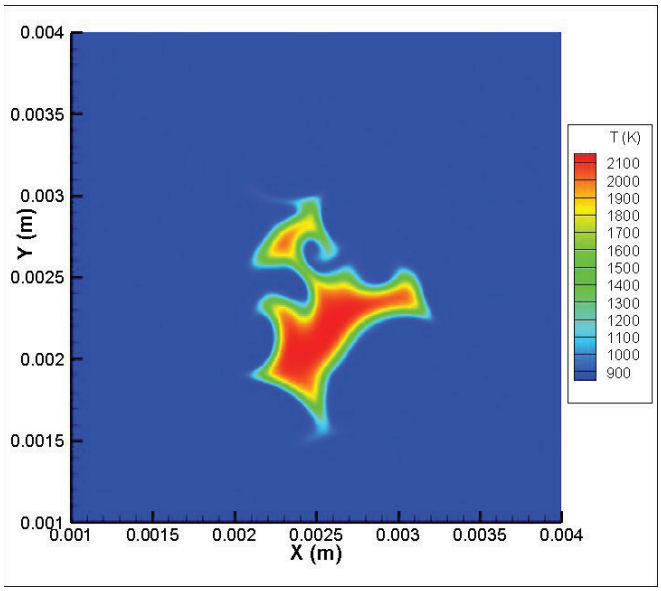

(e)

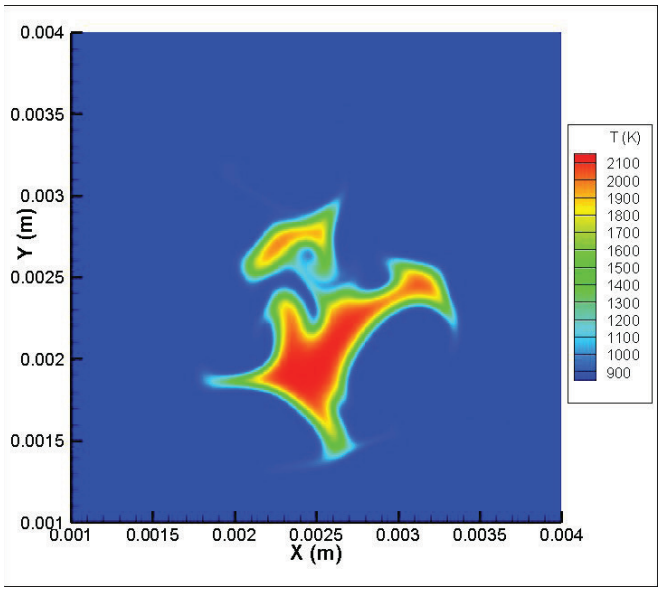

(f)

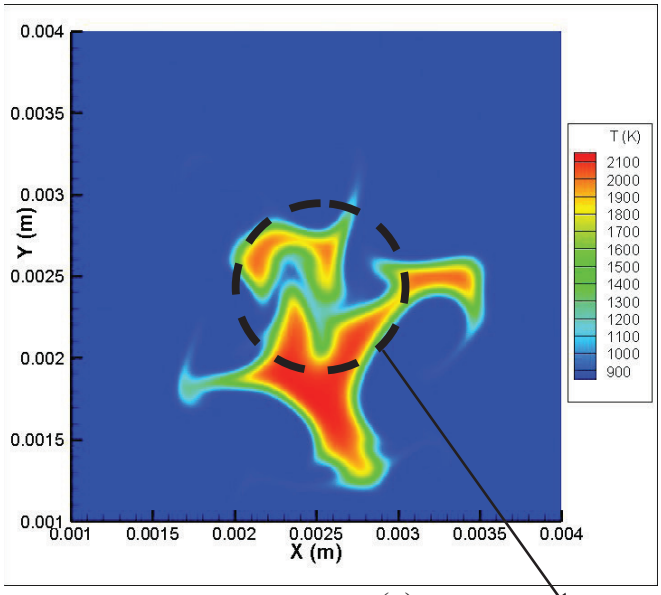

(g)

Initial location of flame kernel

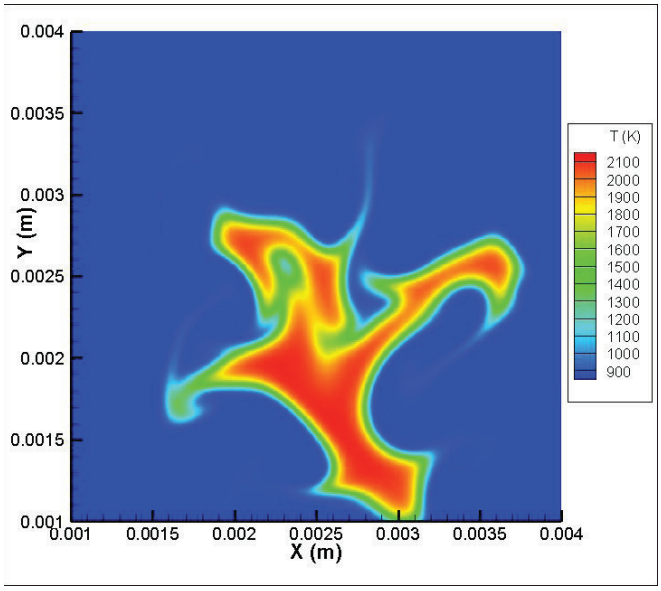

(h)

Fig. 5: Evolution of temperature (K) during the turbulence-kernel interaction with L_I = 0.1 mm, u' = 2 m/s, and d_k=0.5 mm (Case 1 of Table 1) at time t of (a) 0.0, (b) 0.1, (c) 0.2, (d) 0.3, (e) 0.35, (f) 0.5, (g) 0.7, and (h) 0.9 ms.

Figure(s)

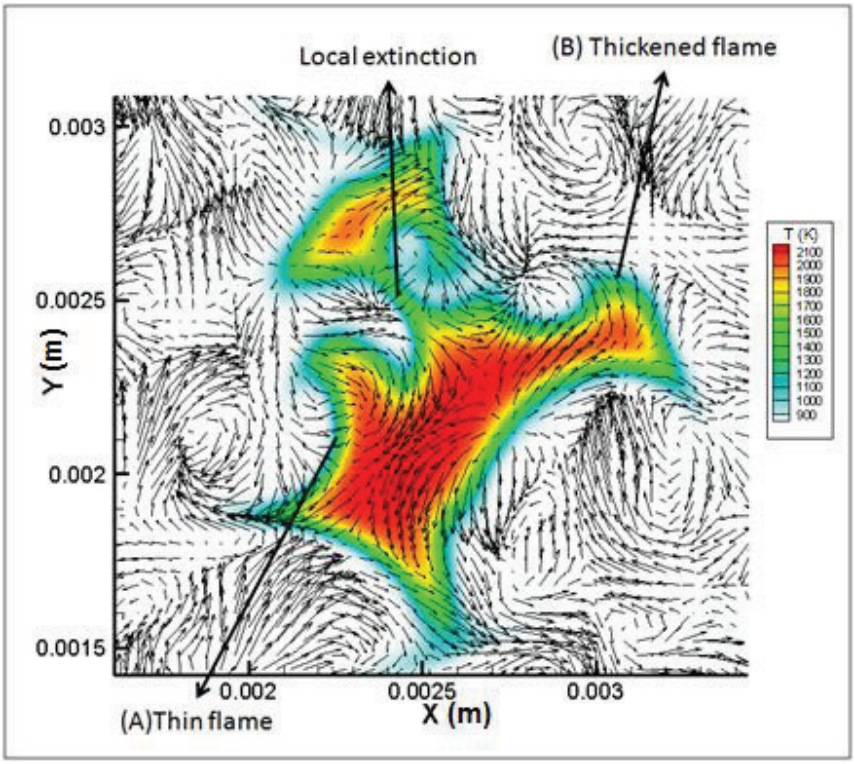

Fig. 6: Velocity vectors overlaid on temperature contours for Case1 at t = 0.4 ms.

Figure(s)

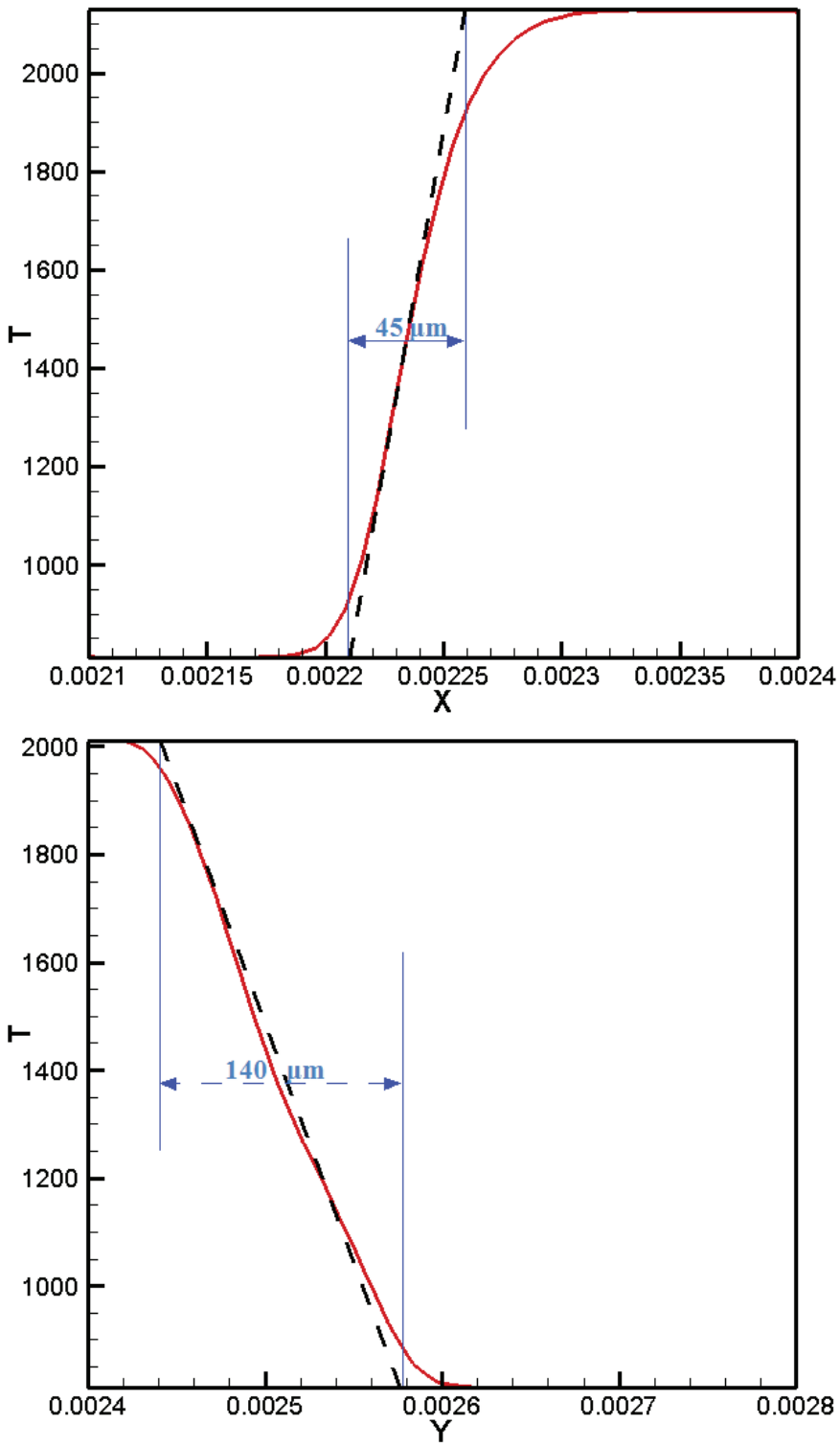

(a) (b)

Figure 7: Temperature as a function of physical distance across two different cross-sections of flame identified as (a) thin flame A and (b) thickened flame B on Fig. 6. The solid line represents

the flame temperature and the dashed line represents the steepest temperature gradient in the flame for comparing the flame thickness.

Figure(s)

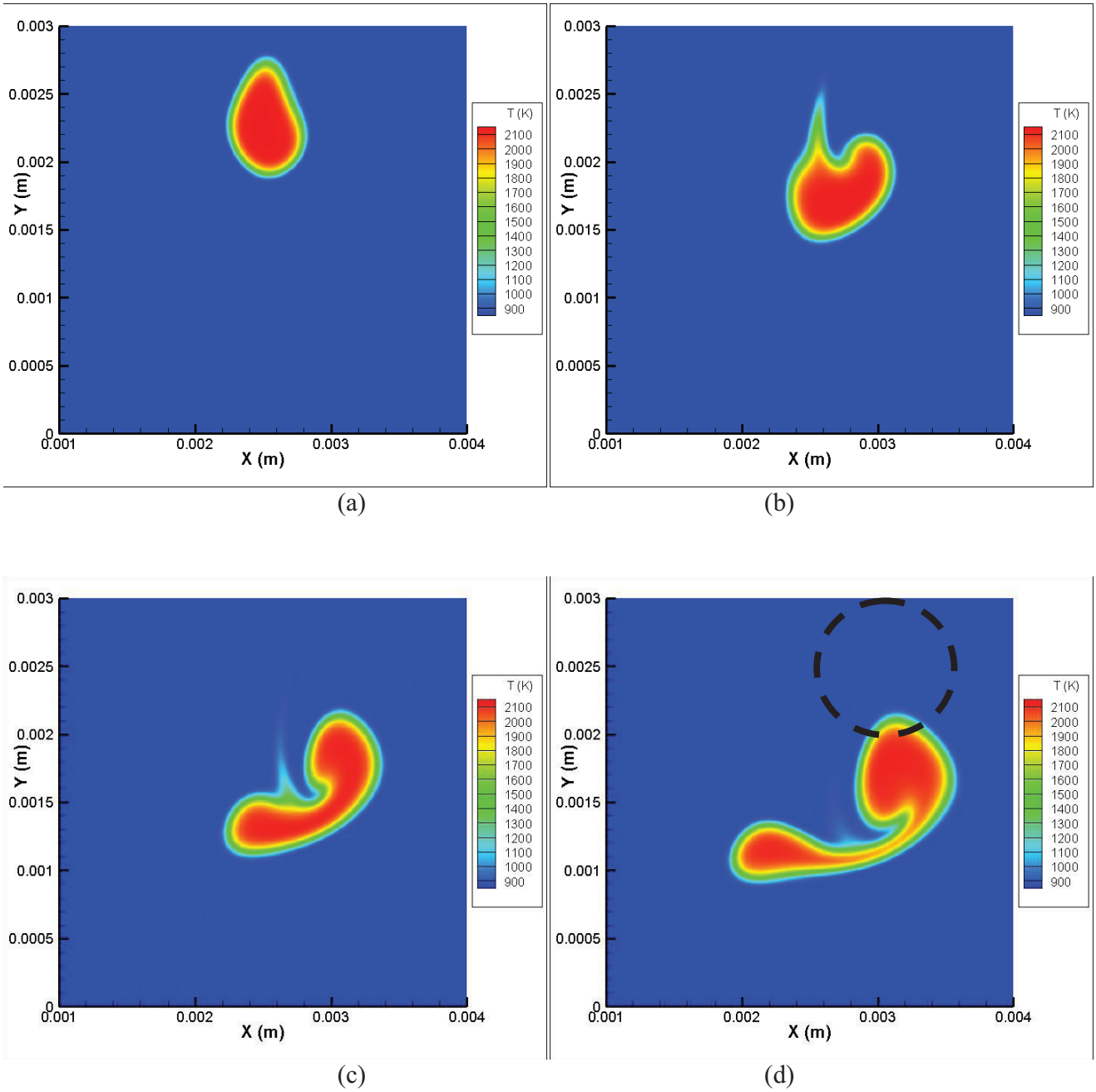

Fig. 8: Evolution of temperature (K) during the turbulence-kernel interaction with L_I = 0.5 mm, u' = 2 m/s, and d_k=0.5 mm (Case 5) at times t of (a) 0.1, (b) 0.3, (c) 0.5, and (d) 0.7 ms.

Figure(s)

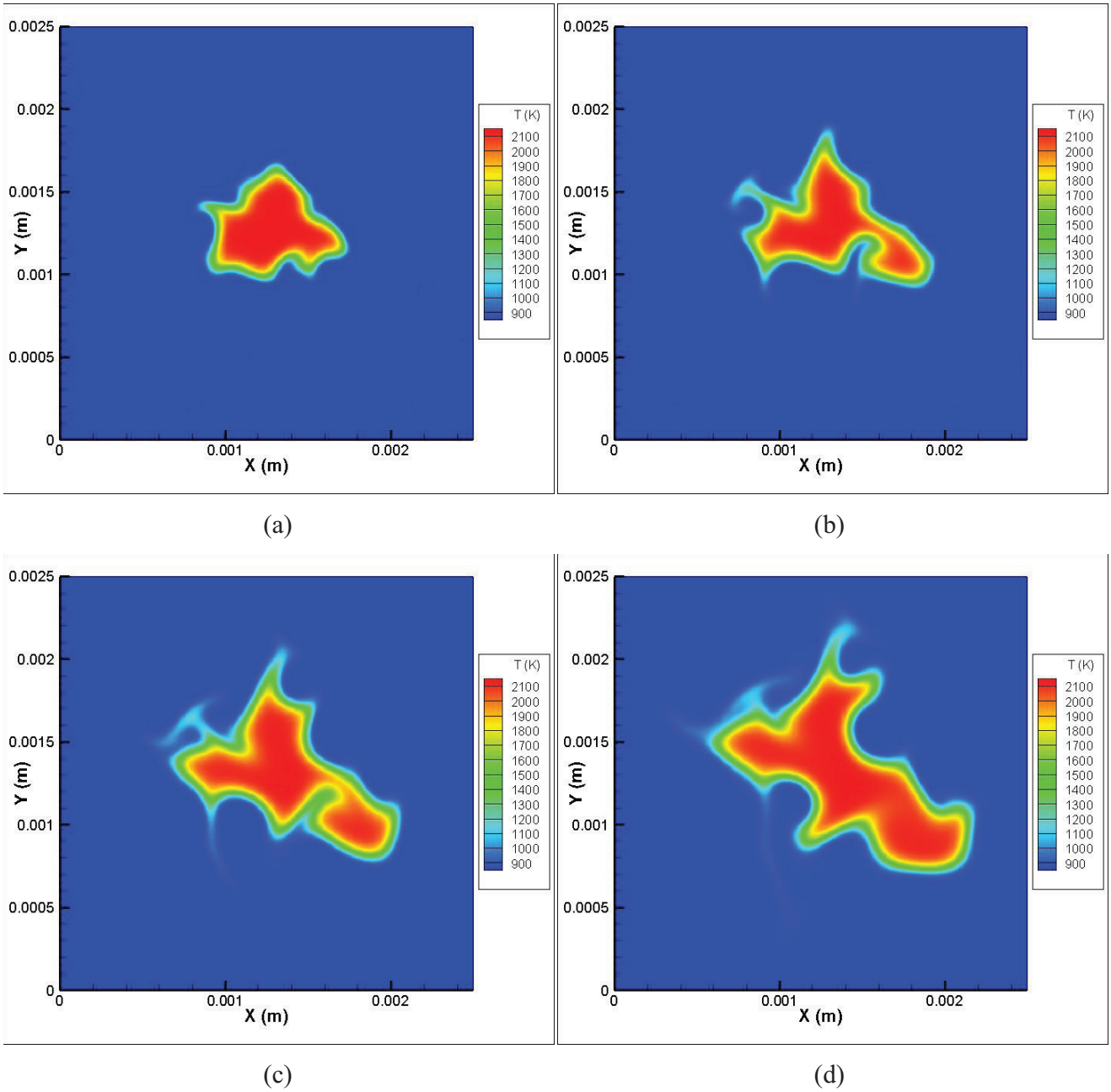

Fig. 9: Evolution of temperature (K) during the turbulence-kernel interaction with $L_I = 0.1$ mm, $u' = 1$ m/s, and $d_k = 0.5$ mm (Case 8) at times t of (a) 0.1, (b) 0.3, (c) 0.5, and (d) 0.7 ms.

Figure(s)

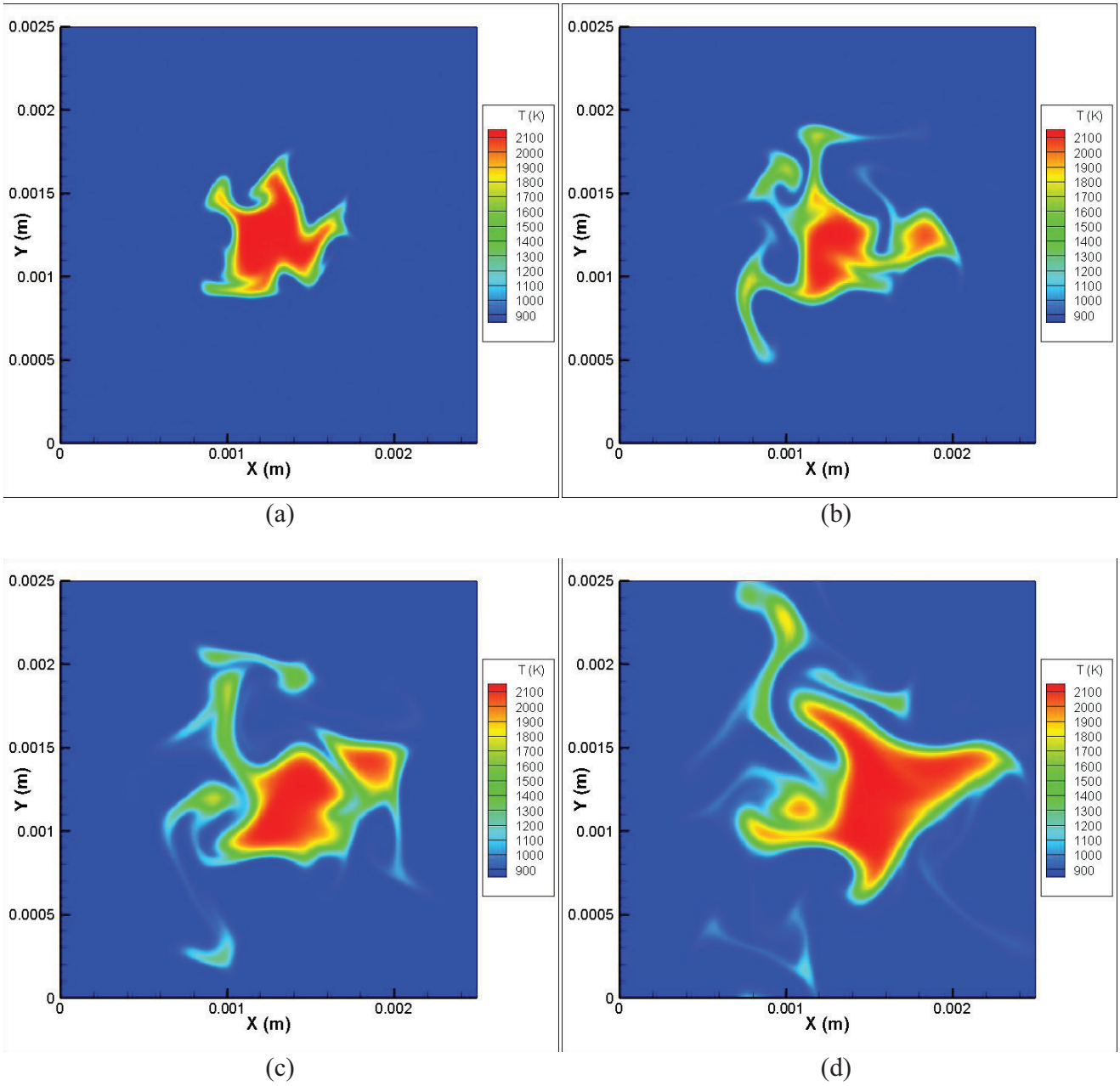

Fig. 10: Evolution of temperature (K) during the turbulence-kernel interaction with $L_I = 0.1$ mm, $u' = 4$ m/s, and d_k=0.5 mm (Case 10) at time t of (a) 0.1, (b) 0.3, (c) 0.5, and (d) 0.7 ms.

Figure(s)

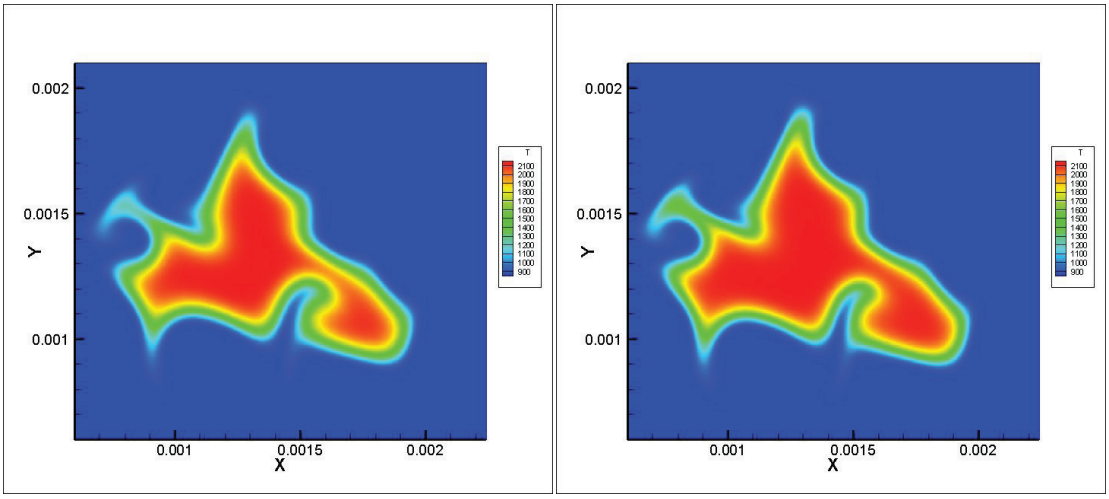

(a) (b)

Fig. 11: Temperature contours (K) during a turbulence kernel interactions where L_I = 0.1 mm, u' = 1 ms, and d_k = 0.5 mm, at t= 0.3 ms for (a) reduced mechanism and (b) single-step mechanism.

Figure(s)

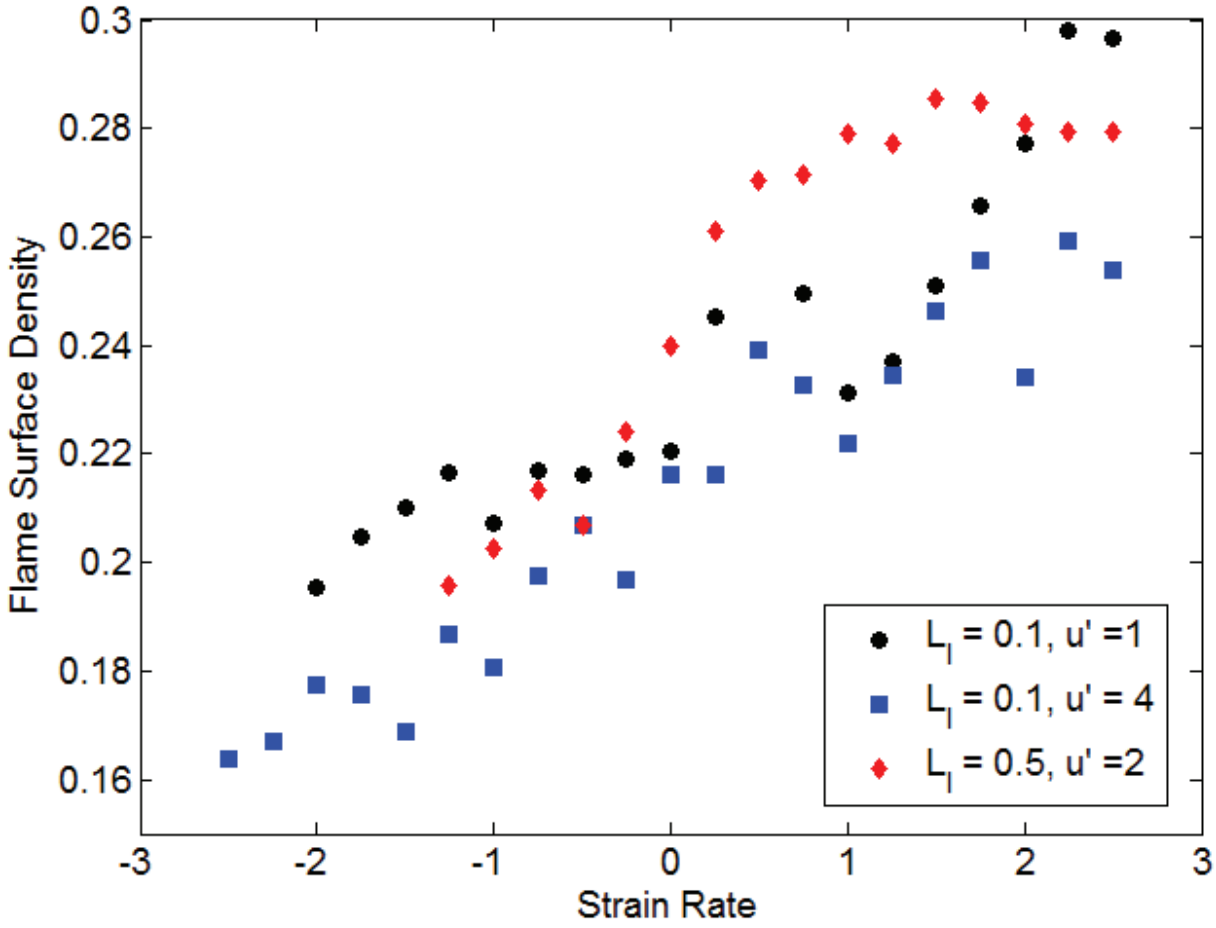

Fig. 12: Variation of normalized flame surface density (Σ x δ_L) with normalized strain rate for Case 5 (L_I = 0.5 mm, u' = 2 m/s), Case 8 (L_I = 0.1 mm, u' = 1 m/s), and Case 10 (L_I = 0.1 mm, u' = 4 m/s).

Figure(s)

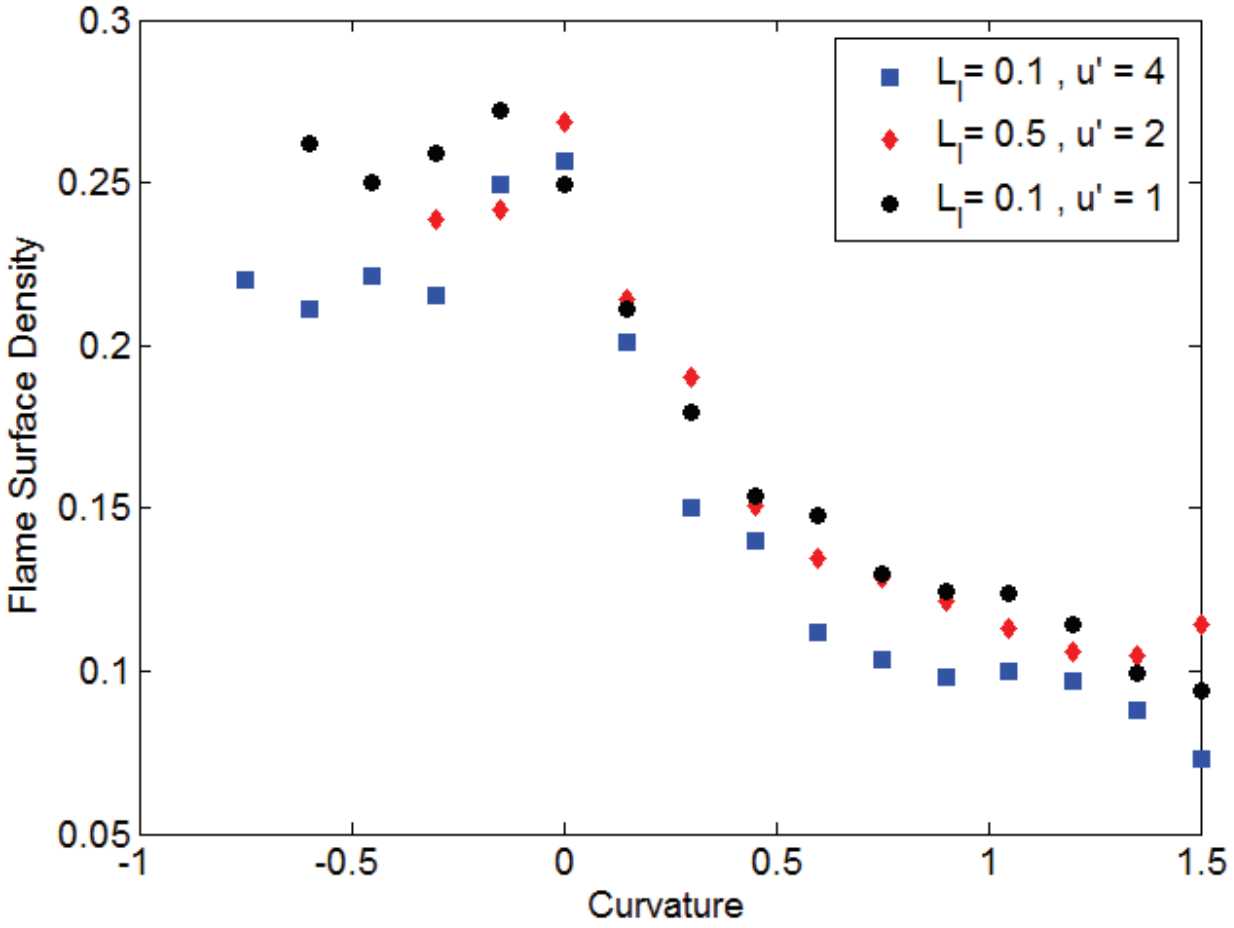

Fig. 13: Variation of normalized flame surface density (Σ x δ_L) with normalized curvature for Case 5 (L_I = 0.5 mm, u' = 2 m/s), Case 8 (L_I = 0.1 mm, u' = 1 m/s), and Case 10 (L_I = 0.1 mm, u' = 4 m/s).

Figure(s)

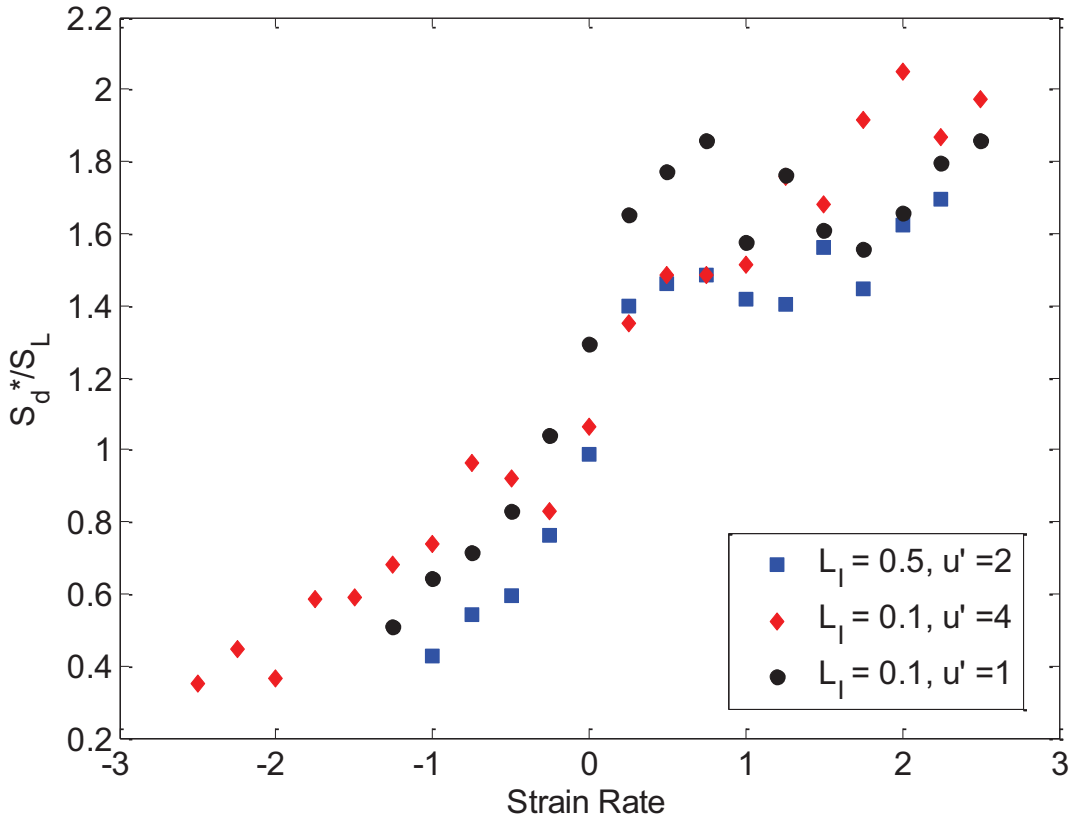

Fig. 14: Variation of normalized local flame speed with normalized strain rate for Case 5 (L_I = 0.5 mm, u' = 2 m/s), Case 8 (L_I = 0.1 mm, u' = 1 m/s), and Case 10 (L_I = 0.1 mm, u' = 4 m/s).

Figure(s)

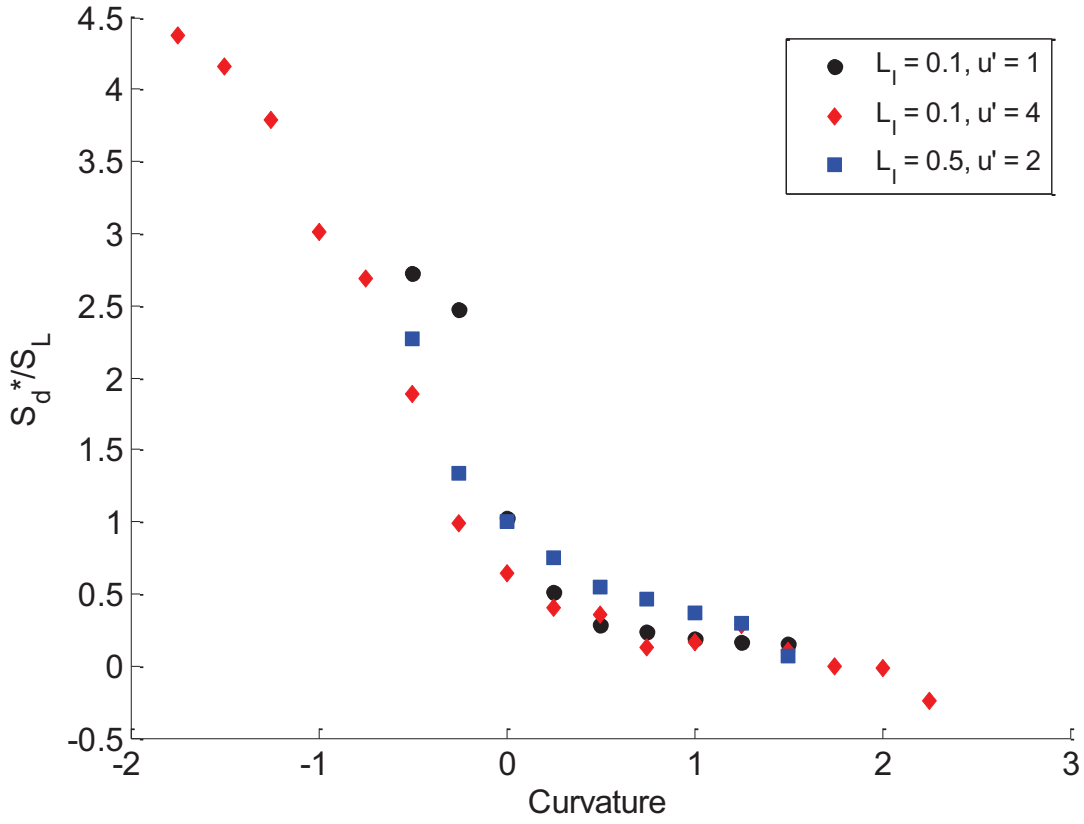

Fig. 15: Variation of normalized local flame speed with normalized flame curvature for Case 5 (L_I = 0.5 mm, u' = 2 m/s), Case 8 (L_I = 0.1 mm, u' = 1 m/s), and Case 10 (L_I = 0.1 mm, u' = 4 m/s).

Figure(s)

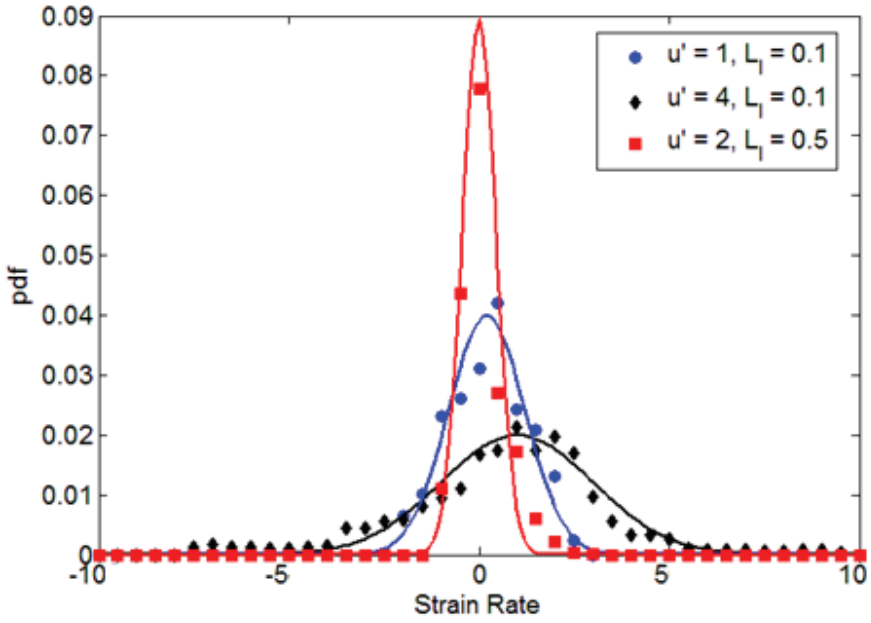

Fig. 16: Strain Rate *pdfs* at a statistically steady state for Case 5 ($L_I = 0.5$ mm, $u' = 2$ m/s), Case 8 ($L_I = 0.1$ mm, $u' = 1$ m/s), and Case 10 ($L_I = 0.1$ mm, $u' = 4$ m/s).

Figure(s)

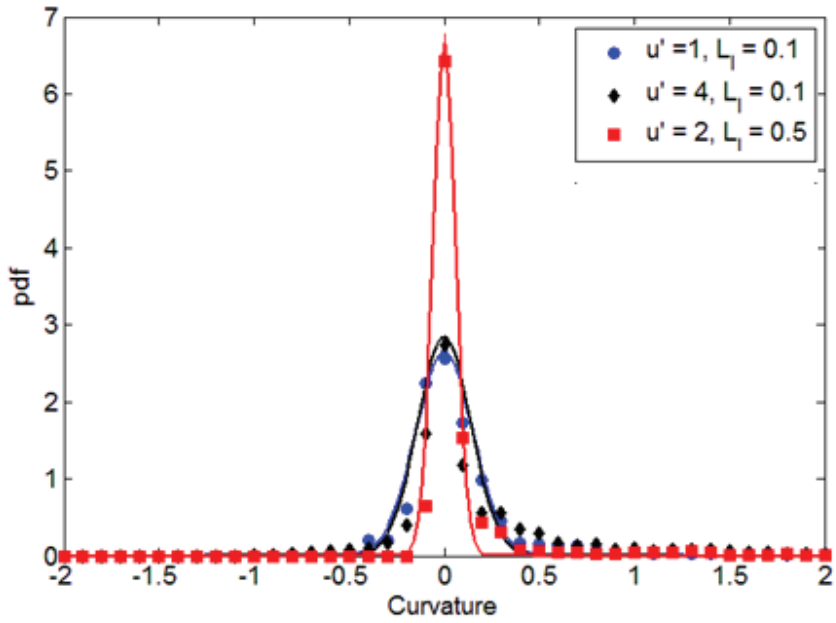

Fig. 17: Curvature *pdfs* at a statistically steady state for Case 5 (L_I = 0.5 mm, u' = 2 m/s), Case 8 (L_I = 0.1 mm, u' = 1 m/s), and Case 10 (L_I = 0.1 mm, u' = 4 m/s).

Figure(s)

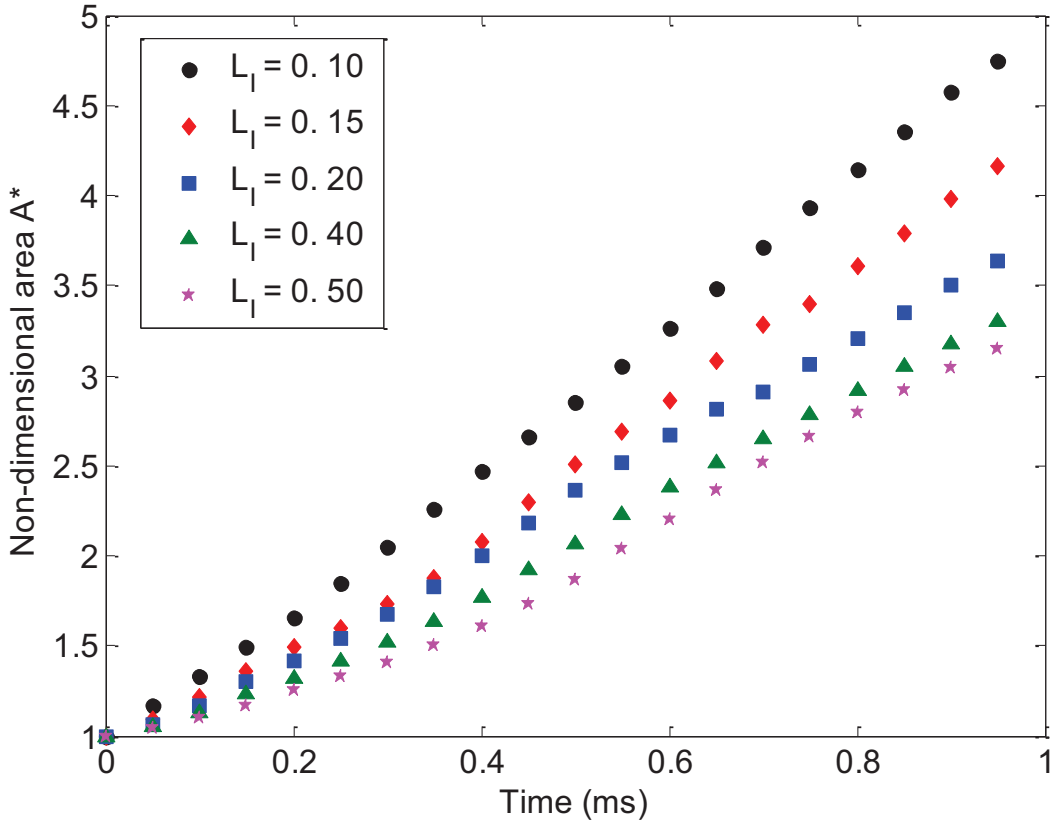

Fig. 18: Variation of non-dimensional flame surface area with time for L_I = 0.10, 0.15, 0.20, 0.40 and 0.50 mm for fixed d_K = 0.5 mm and u' = 2 m/s.

Figure(s)

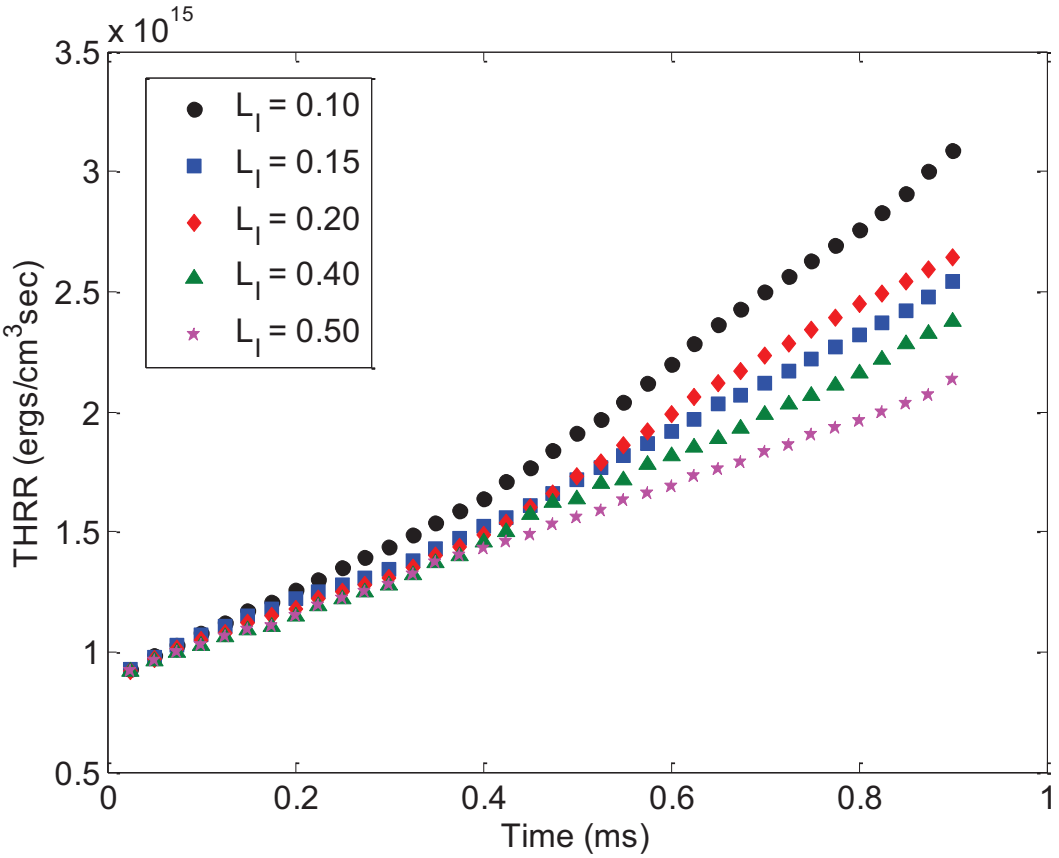

Fig. 19: Variation of total heat release rate (*THRR*) with time for L_I = 0.10, 0.15, 0.20, 0.40 and 0.50 mm for fixed d_K = 0.5 mm and u' = 2m/s.

Figure(s)

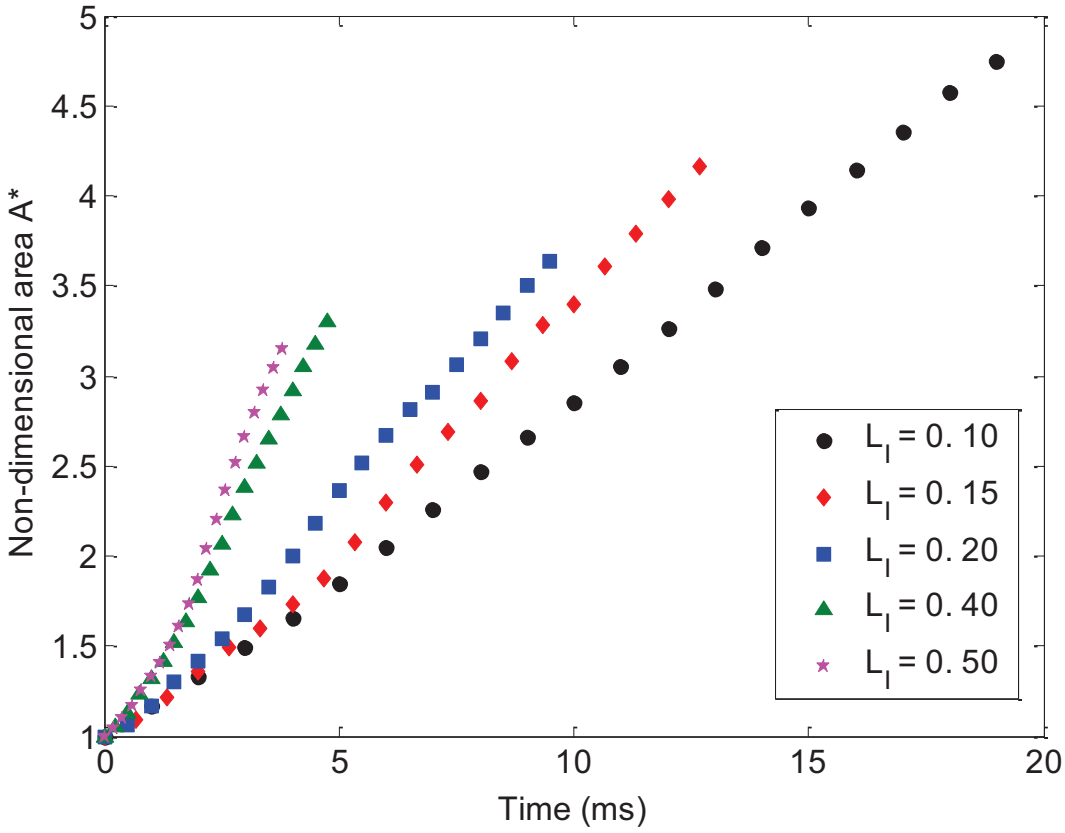

Fig. 20: Variation of non-dimensional flame surface area with number of eddy turn-over times for L_I = 0.10, 0.15, 0.20, 0.40 and 0.50 mm.

Figure(s)

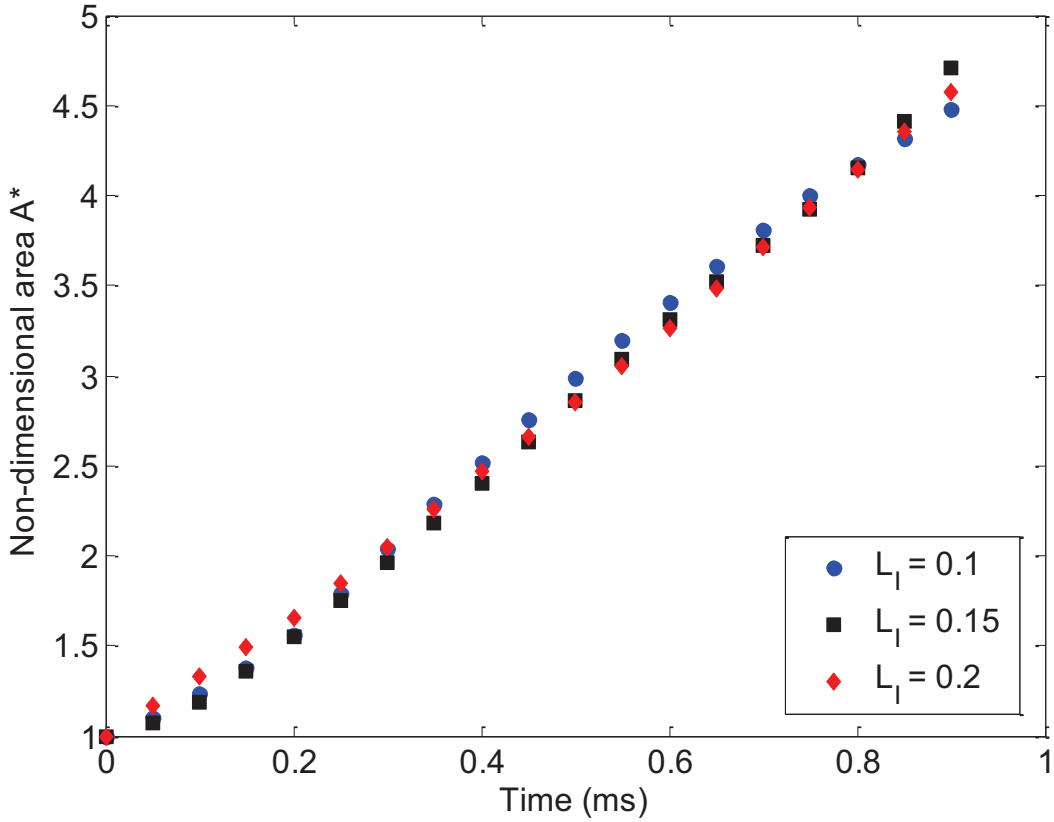

Fig. 21: Variation of non-dimensional flame surface area with time for L_I = 0.10, 0.15 and 0.20 mm for λ = 0.2 and u' = 2 m/s.

Figure(s)

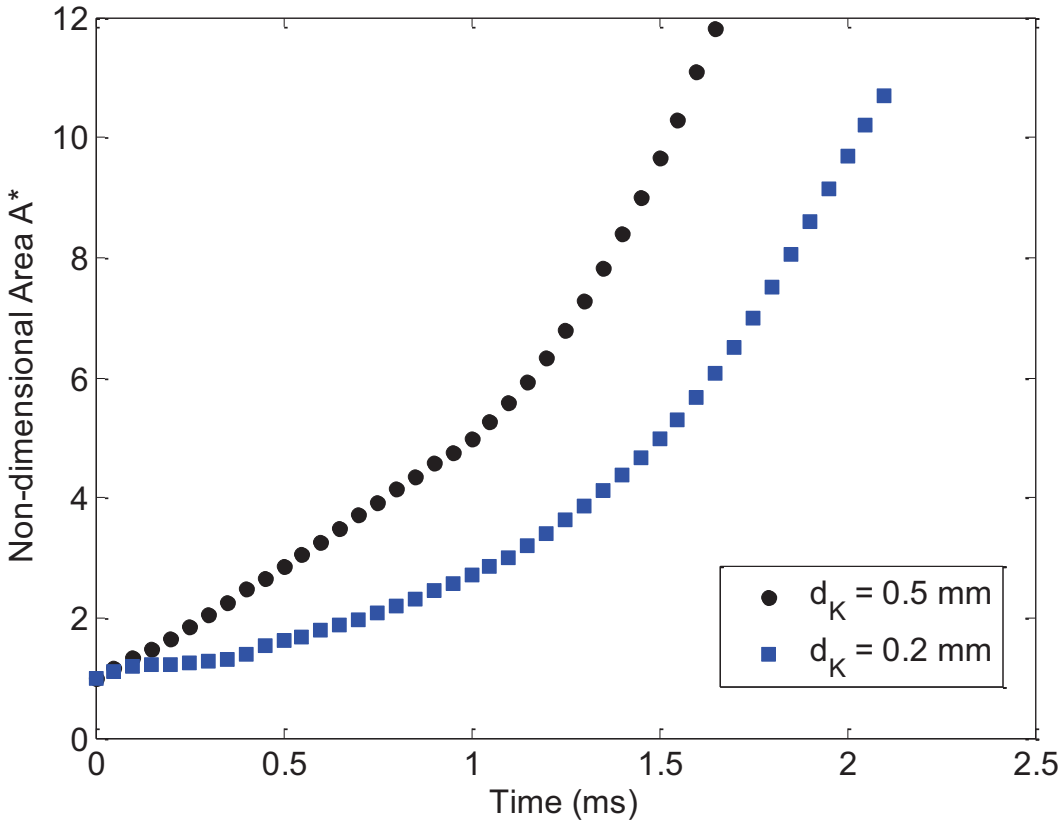

Fig. 22: Variation of non-dimensional flame surface area with time for $\lambda = 0.2$ and $u' = 2$m/s.

Figure(s)

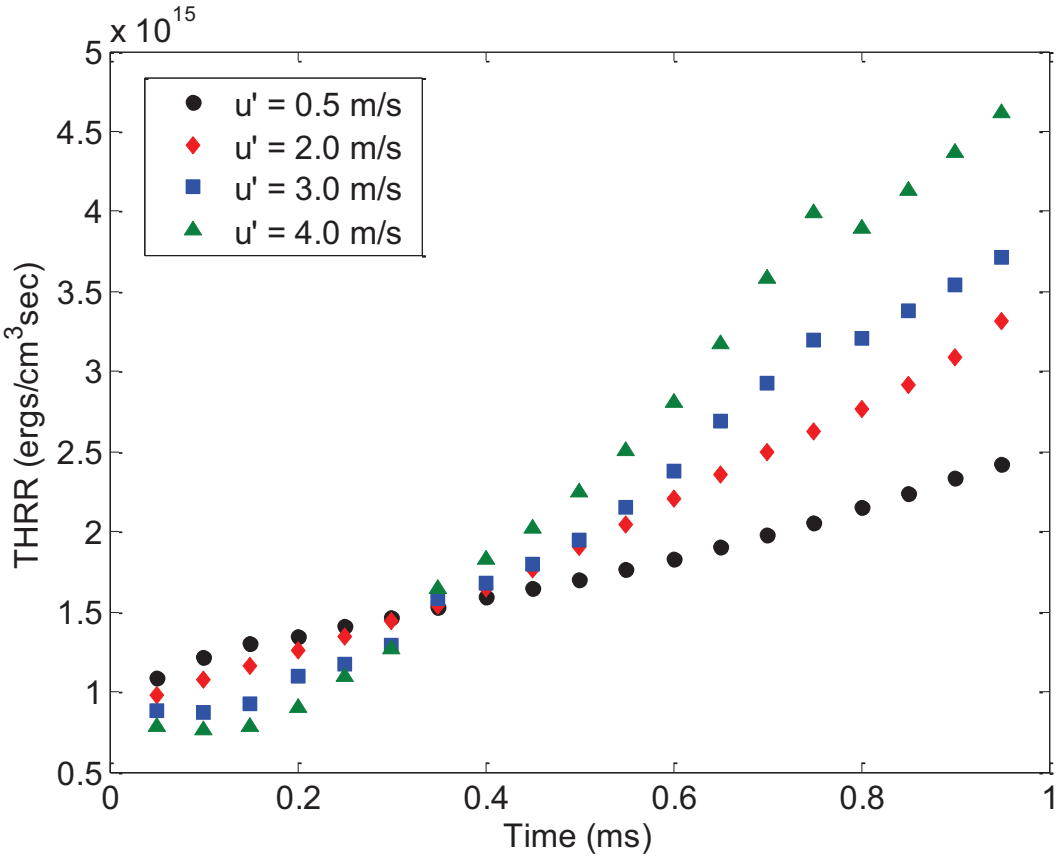

Fig. 23: Variation of total heat release rate (*THRR*) with time for different u' and $L_I = 0.1$ mm.

Figure(s)

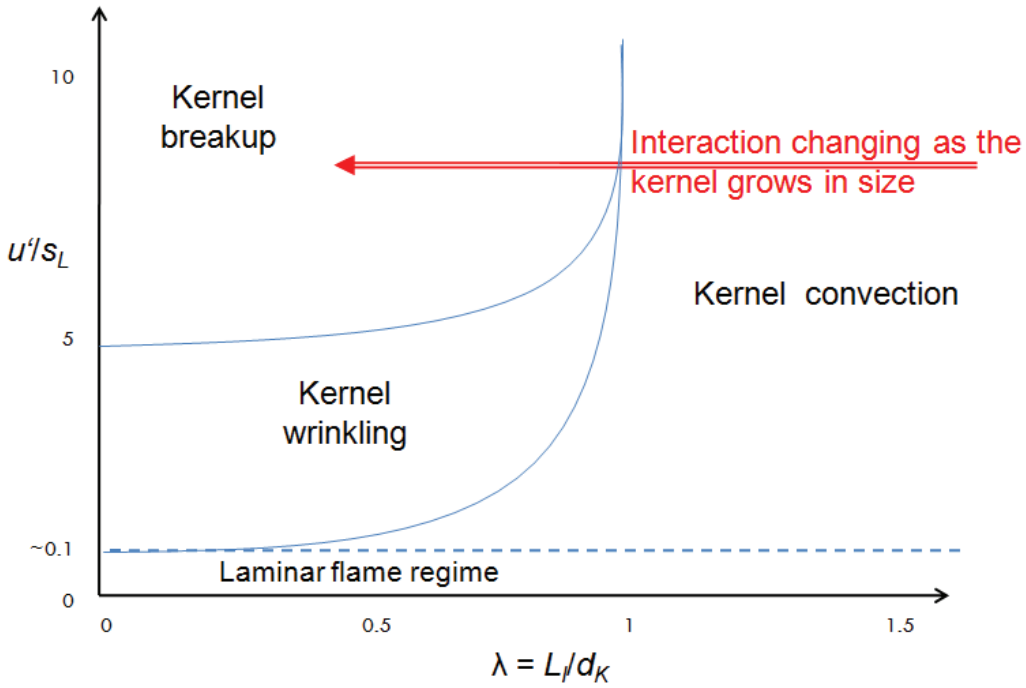

Fig. 24: Turbulence-kernel interaction regime map